Remote Sensing of Cloud Droplet Radius Profiles using solar reflectance from cloud sides. Part I: Retrieval development and characterization

Florian Ewald[1,2], Tobias Zinner[1], Tobias Kölling[1], and Bernhard Mayer[1]

[1]Ludwig Maximilians Universität, Meteorologisches Institut, München, Germany
[2]Deutsches Zentrum für Luft und Raumfahrt, Institut für Physik der Atmosphäre, Oberpfaffenhofen, Germany

Correspondence: Florian Ewald (florian.ewald@dlr.de)

Abstract. Convective clouds play an essential role for Earth's climate as well as for regional weather events since they have a large influence on the radiation budget and the water cycle. In particular, cloud albedo and the formation of precipitation are influenced by aerosol particles within clouds. In order to improve the understanding of processes from aerosol activation, over cloud droplet growth to changes in cloud radiative properties, remote sensing techniques become more and more impor-

5 tant. While passive retrievals for spaceborne observations have become sophisticated and commonplace to infer cloud optical thickness and droplet size from cloud tops, profiles of droplet size have remained largely uncharted territory for passive remote sensing. In principle they could be derived from observations of cloud sides, but faced with with the small-scale structure of cloud sides, 'classical' passive remote sensing techniques are rendered inappropriate. In this work the feasibility is demonstrated to gain new insights into the vertical evolution of cloud droplet effective radius by using reflected solar radiation from

10 cloud sides. Central aspect of this work on its path to a working cloud side retrieval is the analysis of the impact unknown cloud surface geometry has on effective radius retrievals. Using extensive 3D radiative transfer calculations on the basis of realistic droplet size resolving cloud simulations, the sensitivity of reflected solar radiation to cloud droplet size is examined. Sensitivity is enhanced by considering the pixel surrounding to resolve ambiguities caused by illumination and cloud geometry. Based on these findings, a statistical approach is used to provide an effective radius retrieval. An in-depth sensitivity study of

15 the presented approach on the basis of a wide range of radiative transfer test cases demonstrates the feasibility to retrieve cloud particle size profiles from cloud sides.

1 Introduction

1.1 Current state of passive remote sensing of clouds

There exist various methods to infer optical properties (e.g. optical thickness and cloud droplet effective radius) from observa-

20 tion of cloud tops from above using information about the scattered and absorbed radiation in the solar spectrum (e.g., Plass and Kattawar (1968); King (1987)). Phase detection is the first step for every cloud property retrieval. Spectral absorption differences in the near-infrared or brightness temperature differences in the thermal infrared are commonly used to distinguish

Atmospheric
Measurement
Techniques
Discussions

between liquid water and ice (e.g., Nakajima and King (1990)). Various operational techniques exist to retrieve microphysical cloud properties like cloud thermodynamic phase and effective particle size (e.g., Han et al. (1994); Platnick et al. (2001); Roebeling et al. (2006)).

Remote sensing of cloud and aerosol parameters is mostly done by use of multi-spectral sensors, i.e., using only a limited
5   number of spectral bands. Common examples of spaceborne imagers are the Advanced Very High Resolution Radiometer (AVHRR), the Moderate Resolution Imaging Spectroradiometer (MODIS), and the Spinning Enhanced Visible Infrared Imager (SEVIRI). However, there are concerns about measurement artifacts influencing retrievals of aerosol and cloud properties caused by small-scale cloud inhomogeneity which are unresolved by the coarse spatial resolution of spaceborne platforms (Zinner and Mayer, 2006; Marshak et al., 2006b; Varnai and Marshak, 2007).

10   Non-imaging systems like the Solar Spectral Flux Radiometer (SSFR, Pilewskie et al., 2003) or the Spectral Modular Airborne Radiation measurement sysTem (SMART, Wendisch et al., 2001; Wendisch and Mayer, 2003) were used for cloud remote sensing from ground (McBride et al., 2011; Jäkel et al., 2013) or aircraft (Ehrlich et al., 2008; Eichler et al., 2009; Schmidt et al., 2007). The imaging **spec**trometer of the **M**unich **A**erosol **C**loud **S**canner (specMACS, Ewald et al., 2016), is the instrument for which the retrieval in this manuscript has been developed.

15   Marshak et al. (2006a); Martins et al. (2011) proposed cloud side scanning measurements and Zinner et al. (2008); Ewald et al. (2013) presented steps towards a cloud side retrieval for profiles of phase and particle size of convective clouds in order to observe the vertical development of cloud microphysics. Similar to earlier satellite retrievals they propose to use solar radiation in the near-visible to near-infrared spectral regions reflected by cloud sides. Especially the vertical dimension of these observations should reflect many aspects of cloud-aerosol-interaction as well as mixing of cloudy and ambient air (Martins
20   et al., 2011; Rosenfeld et al., 2012). In order to provide a resolved vertical profile a fairly high spatial resolution of the order of 100 m or better is needed. This means that a method has to consider 3D radiative transfer effects.

Albeit sophisticated, the studies of Zinner et al. (2008) and Ewald et al. (2013) are limited to an idealized geometry and simplified cloud microphysics. First, they focus on a space-like perspective for a fixed viewing zenith and scattering angle above the cloud field where sun and sensor have the same azimuth. Therefore, their studies lack the varying geometries of
25   an airborne perspective and avoid the challenge to identify suitable observation positions within the cloud field. Moreover, the spatial resolution of their model cloud fields of 250 m is still rather coarse with respect to an airborne perspective of cloud sides. Second, the effective radius is only parameterized in their studies. For all cloud fields, the effective radius profile is calculated by using a sub-adiabatic ascent of one air parcel in the context of a fixed cloud condensation nuclei concentration. Finally, the approach was not tested for the potential bias to always detect larger effective radii with increasing cloud height; a potential
30   pitfall that could be caused by the prior information contained in the forward calculations.

Since the diverse perspectives and the high spatial resolution of airborne cloud side measurements hampered the application of the approach presented by Zinner et al. (2008) and Ewald et al. (2013) until now, the present work will extend and test their ideas in the context of an airborne perspective. In the course of this part 1, following scientific objectives will be addressed:

1. Extend the existing approach to realistic airborne perspectives and develop methods to test the sensitivity of reflected
35   radiances from cloud sides to cloud droplet radius with the observer position within the cloud field.

Atmospheric
Measurement
Techniques
Discussions

2. Investigate and mitigate 3D radiative effects which can interfere with the proposed cloud side remote sensing technique.

3. Test the approach in the context of realistic and explicit cloud microphysics with a specific focus on potential biases caused by the prior contained in the forward calculations.

Target of this work is the liquid part of convective liquid water clouds, e.g. Cumulus and Cumulus congestus, which exhibit well-developed cloud sides. Part 2 of this work presents an application demonstration to airborne specMACS data collected during the ACRIDICON-CHUVA campaign over Amazonia 2014 Wendisch et al. (2016).

This study is organized as follows: Section 2 shortly recapitulates established methods and introduces the new data set with explicit cloud microphysics. New methods to select suitable cloud sides and connect 3D radiances with 3D cloud microphysics will be described in Section 3. In Section 4, the sensitivity of reflected radiances to cloud droplet radii is examined on the basis of a simple, spherical cloud geometry, before moving the focus to the more realistic cloud side scenes. On the basis of the obtained insights, a method is developed to mitigate 3D radiative effects by using additional information from surrounding pixel. The extensive three-dimensional (3D) radiative transfer simulations of cloud sides, which form the basis of the statistical effective radius retrieval, is described in Section 5. In contrast to previous studies, different aerosol backgrounds are now also considered. Finally, the developed retrieval is tested in Section 6 with unknown scenes of cloud sides, different aerosol backgrounds and analyzed for potential biases.

2 Models

2.1 Statistical approach

The derivation of vertical profiles of cloud microphysics from radiance reflected by cloud sides is a strongly under-determined problem. The statistical approach tries to provide a probability for a specific cloud microphysical state (e.g., effective radius) where a deterministic inversion is impossible due to ambiguities caused by a unknown cloud geometry. This work will follow the approach proposed by Marshak et al. (2006a) and Zinner et al. (2008) who developed a statistical method to account for three-dimensional radiative effects on complex-shaped cloud sides. In their studies, a large number of 3D radiance simulations of cloud data sets provide a database for a statistical effective radius retrieval.

More specific, a forward model is used to perform an ensemble of radiative transfer calculations to estimate the joint probability $p_{\mathrm{fwd}}(L_{0.87}, L_{2.10}, r_{\mathrm{eff}})$ to observe the joint occurrence of radiances $L_{0.87}$, $L_{2.10}$ and effective radius r_{eff}. The likelihood $p(L_{0.87}, L_{2.10} | r_{\mathrm{eff}})$ to observe radiances $L_{0.87}$ and $L_{2.10}$ for a specific effective radius r_{eff} is obtained when the joint probability is normalized with the number of calculations for r_{eff}, the marginal probability $p_{\mathrm{fwd}}(r_{\mathrm{eff}})$. Subsequently, *Bayes' Theorem* is applied to obtain the posterior probability $p(r_{\mathrm{eff}} | L_{0.87}, L_{2.10})$ which solves the inverse problem to retrieve the most likely effective radius r_{eff} when radiances $L_{0.87}$ and $L_{2.10}$ are observed.

Atmospheric
Measurement
Techniques
Discussions

2.2 Monte Carlo approximation

When no analytical expression for the likelihood probability is available, Monte Carlo sampling from the joint distribution can be used to approximate the likelihood and posterior probability (Mosegaard and Tarantola, 1995). Using a radiative transfer model, this sampling yields a histogram $n(L_{0.87}, L_{2.10}, r_{\text{eff}})$ of the frequency of observed radiances $L_{0.87}$ and $L_{2.10}$ and the corresponding effective radius r_{eff}. With the histogram n as a very simple non-parametric density estimator (Scott et al., 1977), the following relation between histogram n and the joined probability $p_{\text{fwd}}(L_{0.87}, L_{2.10}, r_{\text{eff}})$ and marginal probability $p_{\text{fwd}}(r_{\text{eff}})$ can be made:

$$p_{\text{fwd}}(L_{0.87}, L_{2.10}, r_{\text{eff}}) \propto n(L_{0.87}, L_{2.10}, r_{\text{eff}}) \tag{1}$$

$$p_{\text{fwd}}(r_{\text{eff}}) \propto n(r_{\text{eff}}) = \sum_{L_{0.87}} \sum_{L_{2.10}} n. \tag{2}$$

For a successful estimation of these two probabilities, the number of radiative transfer results contained in histogram n needs to be large enough. Simultaneously, the forward simulation has to cover all values expected in the real world application. With the likelihood probability $p(L_{0.87}, L_{2.10}|r_{\text{eff}})$ as a conditional probability, it can be written as the quotient of the joined probability $p_{\text{fwd}}(L_{0.87}, L_{2.10}, r_{\text{eff}})$ and $p_{\text{fwd}}(r_{\text{eff}})$ describing the ensemble of forward calculations contained in n. In this work, the likelihood probability $p(L_{0.87}, L_{2.10}|r_{\text{eff}})$ is approximated by the histogram $n(L_{0.87}, L_{2.10}, r_{\text{eff}})$ which is normalized with $n(r_{\text{eff}})$ using the relations in Equation (1) and Equation (2):

$$p(L_{0.87}, L_{2.10}|r_{\text{eff}}) = \frac{p_{\text{fwd}}(L_{0.87}, L_{2.10}, r_{\text{eff}})}{p_{\text{fwd}}(r_{\text{eff}})} \tag{3}$$

$$p(r_{\text{eff}}|L_{0.87}, L_{2.10}) = \frac{p(L_{0.87}, L_{2.10}|r_{\text{eff}})\, p_{\text{pr}}(r_{\text{eff}})}{\int p(L_{0.87}, L_{2.10}|r_{\text{eff}})\, p_{\text{pr}}(r_{\text{eff}})\, dr_{\text{eff}}} \tag{4}$$

In Equation (3), the prior distribution of r_{eff} in the radiative transfer ensemble is removed by the normalization with the marginal probability $p_{\text{fwd}}(r_{\text{eff}})$. In a final step, the likelihood probability can be used with an arbitrary prior $p_{\text{pr}}(r_{\text{eff}})$ to get the posterior probability $p(r_{\text{eff}}|L_{0.87}, L_{2.10})$ given measurements $L_{0.87}$ and $L_{2.10}$. Hereby, the arbitrary prior $p_{\text{pr}}(\mathbf{m_i})$ must be included within the bounds of the implicit prior $p(r_{\text{eff}})$ in the forward calculations. Values of r_{eff} that are not included in the forward calculations cannot be retrieved since the likelihood probability $p(L_{0.87}, L_{2.10}|r_{\text{eff}})$ is not defined for them. Figure 1 shows how such a Monte Carlo approximation (blue histogram) of a posterior distribution (red line) could look like for given radiance measurements $L_{0.87}$ and $L_{2.10}$. Besides an estimated mean effective radius $\langle r_{\text{eff}} \rangle$, the standard deviation of the posterior distribution also yields the uncertainty connected with this estimate.

2.3 Radiation transport model

The analysis of radiative transfer effects in one-dimensional clouds is done using *DISORT* (Stamnes et al., 1988). The representation of 3D radiative transfer in realistic cloud ensembles is done using the Monte Carlo approach with the *Monte Carlo code for the physically correct tracing of photons in cloudy atmospheres* (*MYSTIC*; Mayer,2009). In order to avoid confusion

Atmospheric
Measurement
Techniques
Discussions
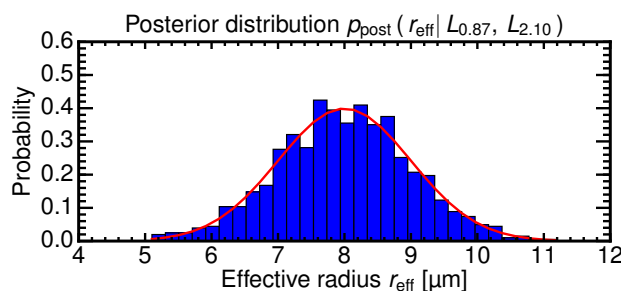
Figure 1. Approximation of a posterior pdf (red) by Monte Carlo Sampling (blue).

with the Monte Carlo sampling of posterior distributions mentioned above, this method will be termed "3D radiative transfer forward modeling" in the following. Both codes are embedded in the radiative transfer library *libRadtran* (Mayer et al., 2005; Emde et al., 2016) which provides prerequisites and tools needed for the radiative transfer modeling. The atmospheric absorption is described by the representative wavelengths absorption parametrization (*REPTRAN*; Gasteiger et al., 2014). This

5 parametrization is based on the HITRAN absorption database (Rothman et al., 2005) and provides spectral bands of different resolution ($1\,\mathrm{cm}^{-1}$, $5\,\mathrm{cm}^{-1}$, and $15\,\mathrm{cm}^{-1}$). Calculations have shown that the spectral resolution of $15\,\mathrm{cm}^{-1}$ (e.g. $\Delta\lambda = 1.1\,\mathrm{nm}$ at $870\,\mathrm{nm}$, $\Delta\lambda = 6.6\,\mathrm{nm}$ at $2100\,\mathrm{nm}$) best suits the spectral resolution of common hyperspectral imagers. The extraterrestrial solar spectrum is based on data from Kurucz (1994) which is averaged over $1.0\,nm$. In order to include vertical profiles of gaseous constituents, the standard summer mid-latitude profiles by Anderson et al. (1986) are used throughout this work. Pre-

10 computations of the cloud scattering phase function and single scattering albedo are done using the Mie tool *MIEV0* from Wiscombe and Warren (1980). When not mentioned otherwise, a Gamma size distribution with $\alpha = 7$ was used for the Mie calculations. The high computational costs of the 3D Monte Carlo radiative transfer method for tracing large numbers of photons are reduced using the *Variance Reduction Optimal Option Method (VROOM)* (Buras and Mayer, 2011), a collection of various variance reduction techniques.

15 **2.4 Cumulus cloud model**

In order to calculate realistic posterior probability distributions $p(r_{eff}|L_{0.87}, L_{2.10})$, likelihood probabilities, produced by a sophisticated forward model, have to be combined with a realistic prior. While Marshak et al. (2006a) used statistical models to obtain this prior of 3D cloud fields, the physical consistency of cloud structures and cloud microphysics are an advantage of the explicit simulation of cloud dynamics and droplet interactions. Following Zinner et al. (2008), this work applies the three-

20 dimensional radiative transfer model MYSTIC to realistic cloud fields which were generated with a *large eddy simulation (LES)* model on a cloud resolving scale. While Zinner et al. (2008) uses realistic cloud structures combined with a bulk microphysics parametrization, this work extends their approach by including explicit simulations of fully consistent, spectral cloud microphysics. In order to cover clean as well as polluted atmospheric environments, LES model outputs with different background cloud condensation nuclei (CCN) concentrations will be used.

This work uses large-eddy simulations of trade wind cumulus clouds. The simulations were initially performed by Graham Feingold in the context of the Rain In Cumulus over Ocean (RICO) campaign (Rauber et al., 2007). The simulations use an adapted version of the Regional Atmospheric Modeling System (RAMS) coupled to a microphysical model Feingold et al. (1996) and described in more detail in Jiang and Li (2009). In addition to the high spatial resolution, cloud microphysics are

5   explicitly represented by size-resolved simulations of droplet growth within each grid box. The cloud droplet distributions cover radii between $1.56\,\mu m$ to $2540\,\mu m$ which are divided into 33 size bins with mass doubling between bins. All warm cloud processes, such as collision-coalescence, sedimentation, and condensation/evaporation are handled by the method of moments developed by Tzivion et al. (1987, 1989). Droplet activation is included by using the calculated supersaturation field and a given cloud condensation nucleus concentration in two versions with $N_{\mathrm{CCN}} = 100\,\mathrm{cm}^{-1}$ and $N_{\mathrm{CCN}} = 1000\,\mathrm{cm}^{-1}$. The LES

10   simulations (*dx25-100* and *dx25-1000*; Jiang and Li, 2009) have a domain size of $6.4 \times 6.4 \times 4\,\mathrm{km}$ with a spatial resolution of $10\,\mathrm{m}$ in the vertical and a spatial resolution of $25 \times 25\,\mathrm{m}$ in the horizontal with periodic boundary conditions. As initial forcing, thermodynamic profiles collected during the RICO campaign (Rauber et al., 2007) were used. With condensation starting at a cloud base temperature of around $293\,\mathrm{K}$ at $600\,\mathrm{m}$, the cloud depth of the warm cumuli varies over a large range from $40\,\mathrm{m}$ to a maximum of $1700\,\mathrm{m}$ (Jiang and Li, 2009).

15   In order to sample a representative prior from this cumulus cloud simulations, a 2 hour $(12\,\mathrm{h} - 14\,\mathrm{h}\,\mathrm{LT})$ model output is sampled every $10\,\mathrm{min}$ for both background CCN concentrations. As input for the following radiative transfer calculations, microphysical moments are derived from the simulated cloud droplet spectra. Effective radius r_{eff}, liquid water content LWC and total cloud droplet concentration N_d can be calculated from mass mixing ratios m_i in $\mathrm{g\,kg}^{-1}$ and cloud droplet mixing ratios n_i in kg^{-1} given for the 33 LES size bins.

20   Figure 2 shows a snapshot of the 3D effective radius field around $12\,\mathrm{h}\,40\,\mathrm{min}\,\mathrm{LT}$ for the case with $N_{\mathrm{CCN}} = 1000\,\mathrm{cm}^{-1}$. In this figure, the full range of LWP and LWC is shown by a logarithmic colormap to highlight their characteristics at cloud edges. With $1067\,\mathrm{g\,m}^{-2}$, the LWP maximum is found co-located with a LWC maximum of over $2\,\mathrm{g\,m}^{-3}$ inside the strongest convective core (Figure 2a). The growth of cloud droplets with height can clearly be seen in the cloud vertical profile (Figure 2b).

As the main object of interest of the retrieval developed herein is thie vertical droplet growth, the range of variation of this

25   process in the cloud data sets is explored in more detail. Figure 3 shows so called contoured frequency by altitude diagrams (CFADs; Yuter and Houze, 1995) for effective radius r_{eff}, liquid water content LWC and total cloud droplet number concentration N_d. Their typical profile is summarized with black lines over all sampled time steps for $N_{\mathrm{CCN}} = 1000\,\mathrm{cm}^{-1}$ and red lines for $N_{\mathrm{CCN}} = 100\,\mathrm{cm}^{-1}$. The frequently occurring low values of N_d and LWC are associated with grid boxes at cloud edges while the wide spectrum of larger values can be found within the cloud cores. As intended the two cloud ensembles cover a

30   wide range of possible values for r_{eff} and N_d between low ("clean") and high CCN concentration ("polluted"). Small droplet r_{eff} and slow growth during ascent characterize the $N_{\mathrm{CCN}} = 1000\,\mathrm{cm}^{-1}$ case, while quick growth to much higher values is present for smaller $N_{\mathrm{CCN}} = 100\,\mathrm{cm}^{-1}$. LWC and cloud lower and upper boundaries show only small differences.

Based on the cloud base droplet number N_{cb}, temperature T_{cb}, pressure and a saturation adiabatic lapse rate (here we assume $4\,\mathrm{K\,km}$), "adiabatic" reference values can be calculated for an ensemble of droplets growing by condensation during ascent

35   neglecting entertainment of dry environmental air (broken lines). The existence of other effects (e.g. entrainment, coalecence)

Atmospheric
Measurement
Techniques
Discussions
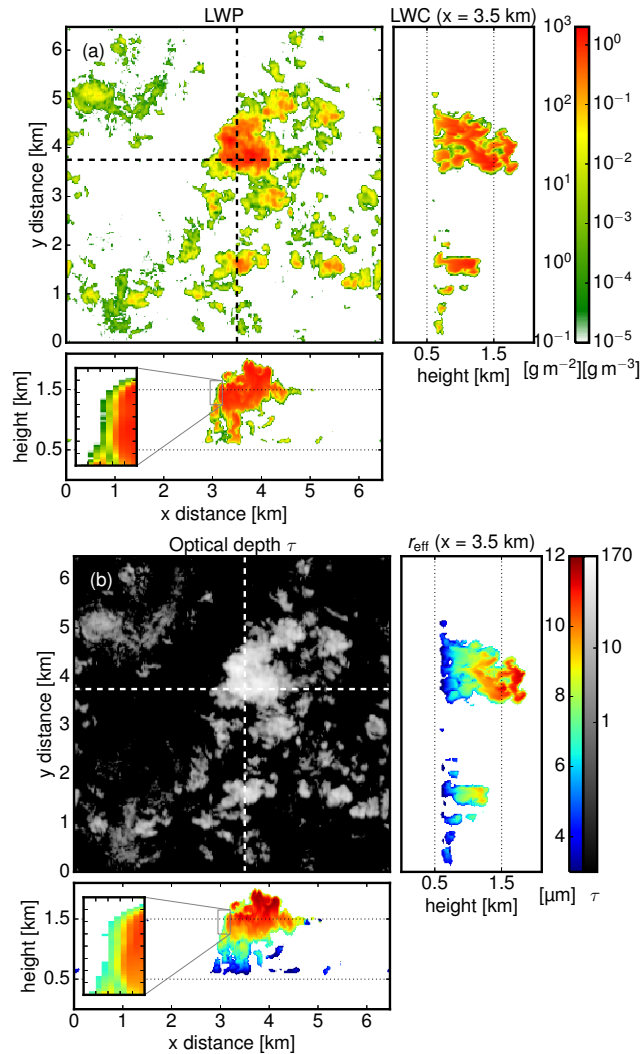
Figure 2. (a) Liquid water path in $\mathrm{g\,m^{-2}}$ and vertical cross-sections of liquid water content in $\mathrm{g\,m^{-3}}$ at $x = 3.5\,\mathrm{km}$ and $y = 2.75\,\mathrm{km}$ for the LES cloud field around $12\,\mathrm{h}\,40\,\mathrm{min}$ LT. **(b)** Corresponding optical thickness τ and vertical cross-sections of effective radius r_{eff} for the same cloud scene. Zoomed cut-outs contain cross-sections of r_{eff} and LWC for a cloud edge region showing signs of lateral entrainment.

becomes evident in comparison with the modeled LWC and N_d profiles, as the adiabatic theory provides only an upper limit to their values. In contrast, r_{eff} follows the adiabatic limit more closely with sub-adiabatic values between $60 - 80\%$ which is in accordance with in-situ aircraft observations during the RICO campaign (Arabas et al., 2009) and other studies (Martin et al., 1994).

Atmospheric
Measurement
Techniques

Open Access

Discussions
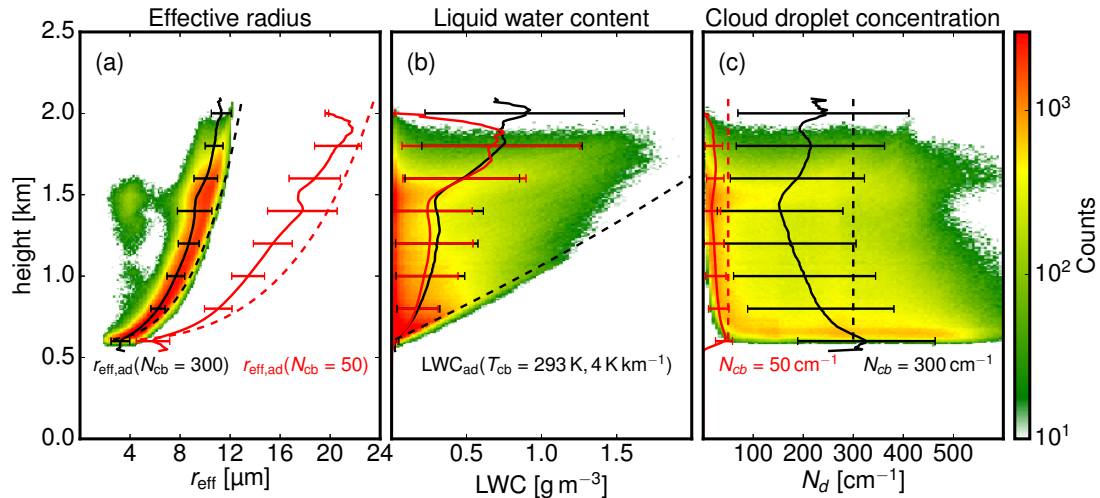
Figure 3. Contoured frequency by altitude diagrams (CFADs) of **(a)** effective radius r_{eff}, **(b)** liquid water content LWC and **(c)** cloud droplet number concentration N_d for $N_{\text{CCN}} = 1000\,\text{cm}^{-1}$. The respective mean profile (black solid line) and its standard deviation (error bar) are superimposed, results for $N_{\text{CCN}} = 100\,\text{cm}^{-1}$ are shown in red. The dashed profile is the theoretical adiabatic limit calculated for conditions at cloud base ($T_{\text{cb}} = 293\,\text{K}, N_{\text{cb}} = 300\,\text{cm}^{-1}, 4\,\text{K}\,\text{km}^{-1}$).

3 Methods

3.1 Selection of suitable cloud sides

A key component of the Bayesian approach is the selection of a suitable sampling strategy to explore the likelihood distribution $p_{\text{fwd}}(L_{0.87}, L_{2.10} | r_{\text{eff}})$. This is especially true, if the sampling of the observation parameter space is done with a computational

5   expensive 3D radiative transfer method. Following Mosegaard and Tarantola (1995), the sampling of the model space can be improved when the model space is sampled with the intended measurements in mind. Instead of sampling the radiative transfer in 3D cloud fields completely at random, the indented measurement location and perspective should be taken into account.

To that end, the we introduce a technique to select suitable locations within the LES model output for which cloud sides are visible from the airborne perspective. Cloud side measurements are intended for clouds within several kilometers from

10   the instrument location. With the sun in the back, azimuthal positions of $\pm 45°$ around the principal plane will be accepted for an airborne field of view which is centered slightly below the horizon. To ensure reproducibility, an analytical method is chosen to select observation locations to sample the likelihood distribution. The field-of-view is modeled by an observation kernel k_{FOV} with an azimuthal opening angle of $\Delta\varphi = 45°$ and a zenithal opening angle of $\Delta\vartheta = 40°$, centered around $5°$ below the horizon. As a function of radial distance, the observation kernel comprises a scalar weighting to curtail the location

15   where clouds are desired. Figure 4 shows a vertical cross-section of this kernel. The arbitrary score is strongly negative in the vicinity of the observer to penalize locations where clouds are too close. Observation distances of $3\,\text{km}$ to $5\,\text{km}$ turned out to maximize the likelihood to observe a complete cloud side in the used LES model output. For a distance of $2\,\text{km}$ and onward,

Atmospheric
Measurement
Techniques
Discussions

Open Access
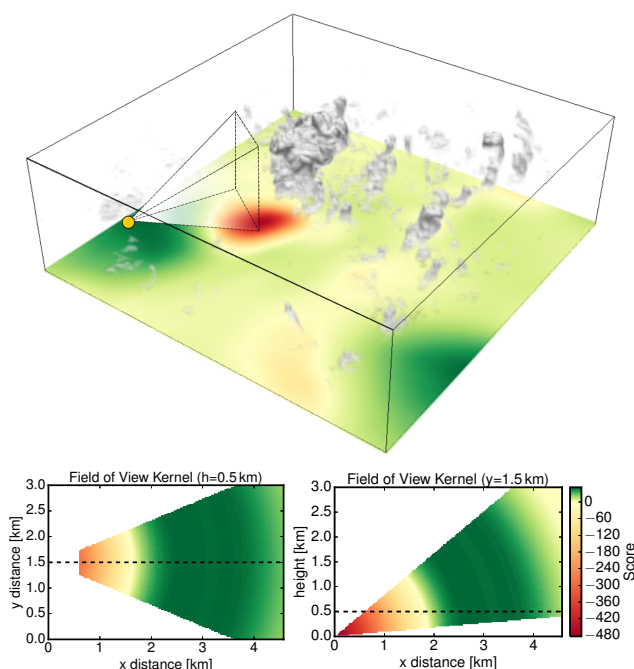
Figure 4. (a) Finding the optimal observation location for cloud side measurements. The surface shows the location score derived by convolving the observation kernel (shown in Figure 4) with the LES cloud field $(12\,h\,40\,min\,LT)$ shown in Figure 2 **(b)** Vertical cross-section within the principal plane of the observation kernel. The arbitrary score is positive for regions where clouds are desired.

the weighting score becomes thus positive with a maximum at $3.5\,km$ to favor locations with clouds in this region. For all LES cloud fields on average, this method positions the observer at a distance of around $4\,km$ from cloud sides.

Subsequently, the field of cloudy grid boxes is convolved with the observation kernel at an observation altitude of $h = 1.7\,km$, creating a two-dimensional score field s_{obs}. For every cloud field and chosen azimuthal orientation, the observation position
5   is then placed where s_{obs} has its global maximum. In Figure 4a, the already introduced LES cloud field $(12\,h\,40\,min\,LT)$ is shown in combination with the corresponding score field s_{obs} obtained for a viewing azimuth of $\phi = 315°$. The observation position is indicated by the yellow dot, where s_{obs} has its global maximum as recognizable by the green color. Also depicted is the field of view towards the largest cloud in the center of the domain. The red region in s_{obs} would be unfavorable for a cloud side perspective since it would be too close to the cloud. For the selected perspective shown in Figure 4a, a simulated truecolor
10 image is shown in Figure 5a.

Determination of the apparent effective radius

In their statistical retrieval approach, Zinner et al. (2008) traced along the line of sight of each individual sensor pixel until hitting the first cloudy model grid box from which they selected their r_{eff} corresponding to the observed radiances. This

Atmospheric
Measurement
Techniques
Open Access
Discussions
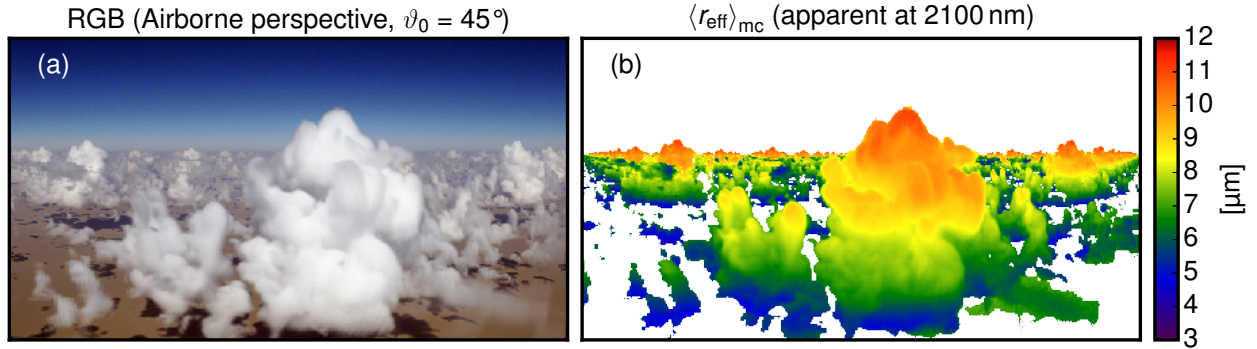
Figure 5. (a) Truecolor image of a scene selected. **(b)** Apparent effective radii $\langle r_{\mathrm{eff}} \rangle_{mc}$ obtained with MYSTIC REFF for the same scene.

method has its limitations when it comes to highly structured cloud sides with horizontally inhomogeneous microphysics. By neglecting the penetration depth of photons, reflection from deeper within the cloud are disregarded. Radiance observations at given wavelengths can not carry the information from this first grid box alone, but from the full multi-scattering path. The found effective radius r_{eff} therefore becomes biased towards droplet sizes found directly at cloud edges. However, due to very
5   low LWCs, these grid boxes have only a marginal contribution to the overall reflectance.

As Platnick (2000) showed, the penetration depth of reflected photons in the visible spectrum lies within some hundred meters while in the near-infrared spectrum the penetration depth is only a few dozen meters. The co-registration of responsible cloud droplet sizes with modeled radiances is essential. Besides the observation perspective, this *apparent effective radius* $\langle r_{\mathrm{eff}} \rangle_{app}$ also depends on the observed wavelength since different scattering and absorption coefficients lead to different cloud
10   penetration depths.

As discussed by Platnick (2000), there exist analytical as well as statistical methods to consider the contribution of each cloud layer to the apparent effective radius $\langle r_{\mathrm{eff}} \rangle_{app}$. Advancing the one-dimensional weighting procedures of Platnick (2000) and Yang et al. (2003), the 3D tracing of photons in MYSTIC is utilized to calculate the optical properties of inhomogeneous, mixed-phase clouds. The apparent effective radius $\langle r_{\mathrm{eff}} \rangle_{app}$ for a photon can be described as a weighted, linear combination
15   (Equation (5)) of the individual effective radii r_{eff} the photon encounters on its path through the cloud:

$$\langle r_{\mathrm{eff}} \rangle_{app} = \frac{\int_0^l k_{ext}(l')\, r_{\mathrm{eff}}(l')\, dl'}{\int_0^l k_{ext}(l')\, dl'}, \tag{5}$$

In Equation (5), the effective radii are weighted with the corresponding extinction coefficient k_{ext} of the cloud droplets along the path length in each grid box. Subsequently, the mean over all photons traced for one forward simulated pixel leads to the apparent effective radius $\langle r_{\mathrm{eff}} \rangle_{mc}$ of this pixel:

$$20 \quad \langle r_{\mathrm{eff}} \rangle_{mc} = \frac{\sum_{i=0}^{photons} p_{w,i}\, \langle r_{\mathrm{eff}} \rangle_{app}}{\sum_{i=0}^{photons} p_{w,i}}. \tag{6}$$

Atmospheric
Measurement
Techniques
Discussions
Open Access
EGU

In the summation Equation (6), the photon weight $p_{w,n}$ is used to account for the different photon path probabilities. As the photon weights $p_{w,n}$ are also used in the calculation of $L_{0.87}$ and $L_{2.10}$, the apparent effective radius $\langle r_{\text{eff}} \rangle_{mc}$ can be derived simultaneously. This method was integrated within the MYSTIC 3D code and will therefore be referred to as the *MYStic method To Infer the Cloud droplet EFFective Radius (MYSTIC REFF)*. For the cloud scene shown in Figure 5a, Figure 5b shows the apparent effective radius $\langle r_{\text{eff}} \rangle_{mc}$ obtained with MYSTIC REFF. Compared with the effective radius found at the cloud edge, $\langle r_{\text{eff}} \rangle_{mc}$ appears much smoother. The vertical gradient of $\langle r_{\text{eff}} \rangle_{mc}$ also compares better with the vertical gradient of effective radii r_{eff} shown in Figure 3b. The method shows very good agreement with the analytical solution of Yang et al. (2003) for homogeneous mixed-phase clouds and Platnick (2000) for one-dimensional clouds with a vertical effective radius profile.

4 The cloud geometry effect and its mitigation

Reflected radiance at non-absorbing wavelengths is mainly influenced by optical thickness and by the amount of radiation incident on the cloud surface. For the latter, cloud surface orientation with respect to the sun is decisive. This is a problem for all retrievals using this radiance to derive τ_c or, in combination with an absorbing wavelength, τ_c and r_{eff} (Nakajima and King, 1990) in all situations with unknown (non-plane-parallel) clouds. In such a situation, e.g. for cloud side observations, the limitation to optically thick clouds can be a way out. With increasing optical thickness τ_c, the solar cloud reflectance becomes less sensitive to variations of τ_c. In contrast to the typical observation geometry from above where a plane-parallel cloud is assumed, cloud surface orientation is unknown and only the scattering angle ϑ_s is known. In the following study, the ambiguity caused by the unknown cloud surface orientation and the remaining sensitivity to the effective radius will be explored. Molecular absorption and scattering will be neglected in the following idealized study.

4.1 Ambiguities of reflected radiances

Figure 6 shows the basic geometry for cloud side remote sensing. The normal which defines the cloud surface is $\hat{\mathbf{n}}$, the vector pointing from sun into direction of light propagation is denoted with $\hat{\mathbf{s}}$ and the vector pointing into direction of the observer is denoted with $\hat{\mathbf{v}}$. The viewing zenith angle ϑ and the sun zenith angle ϑ_0 are still referenced within the global coordinate system which is defined parallel to the ground. Corresponding to these two angles, two additional angles exist which describe the inclination of $\hat{\mathbf{s}}$ and $\hat{\mathbf{v}}$ on the oriented cloud surface: the local illumination angle ϑ_0^* and the local viewing angle ϑ^* with respect to the cloud surface. In a first step, all vectors are assumed to be within the principal plane (the plane spanned by $\hat{\mathbf{s}}$ and $\hat{\mathbf{n}}$). Figure 6 shows two different viewing geometries of a vertically-oriented cloud surface under the same local illumination angle ϑ_0^*. For both cases, Figure 7 shows spectral radiances at $\lambda = 870\,\text{nm}$ and $\lambda = 2100\,\text{nm}$ for a clockwise rotation of the cloud surface. The radiative transfer calculations were done with DISORT for an optically thick ($\tau = 500$) water cloud with a fixed r_{eff} of $9\,\mu\text{m}$. The arrows in Figure 7 indicate the progression of radiance values, as it could be observed during a cloud surface rotation within the principal plane as shown in Figure 6. The figure uses a typical two-channel diagram with the absorbing channel on the x-axis and the non-absorbing on the y-axis. E.g. Nakajima and King (1990) use this form to present
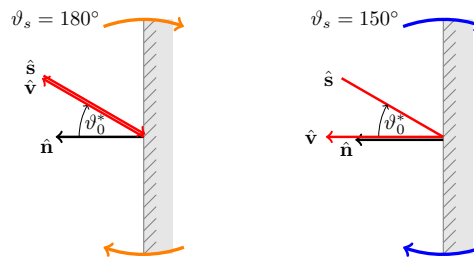
Figure 6. Two observation geometries with a scattering angle of $\vartheta_s = 180°$ **(left)** and $\vartheta_s = 150°$ **(right)**. Same cloud surface orientation $\hat{\mathbf{n}}$ (cloud surface normal) and illumination $\hat{\mathbf{s}}$ (solar direction vector) but different local viewing angle ϑ^*. The impact of the indicated cloud surface rotation on reflected radiances is shown in Figure 7

the dependence of reflected radiance in both channels on the systematic variation of τ and r_{eff} values for plane-parallel clouds (hereafter denoted as "2-wavelength retrieval" and "2-wavelength diagram"). The similarity of these lines to the isolines for fixed r_{eff} and varying τ in their diagrams is striking.

Nakajima and King (1990) use the radiance in the non-absorbing wavelength to infer the optical thickness τ. Numerous
5 studies Cahalan et al. (1994); Varnai and Marshak (2002); Zinner and Mayer (2006); Vant-Hull et al. (2007) pointed out, that tilted and therefore more shadowed or illuminated cloud sides have a huge impact on the retrieval of optical thickness.The radiance similarity of cloud surface rotation and optical thickness variation further underlines the necessity to restrict the retrieval to optically thick clouds when the cloud surface orientation is unknown. Therefore, the following analysis will determine the remaining information content in $L_{0.87}$ and $L_{2.10}$ about r_{eff} for optically thick clouds with an unknown cloud surface
10 orientation.

A difference between the direct backscatter case with a scattering angle of $\vartheta_s = 180°$ and the case with a scattering angle of $\vartheta_s = 150°$ becomes already evident in Figure 7. While the spectral radiance first increases at both wavelengths as the local illumination and viewing angle becomes smaller, it is only in case of direct backscatter that spectral radiances decrease the same way as they increased when the illumination angle becomes more oblique again. In case of scattering angle $\vartheta_s = 150°$, as
15 long as the local viewing angle ϑ^* is smaller than the local illumination angle ϑ_0^*, spectral radiances at $\lambda = 2100\,\mathrm{nm}$ are lower than for the remaining part of the rotation when $\vartheta^* > \vartheta_0^*$. Within the principal plane, a rotation of the cloud surface produces a characteristic bow structure for scattering angles $\vartheta_s < 180°$ (evident in Figure 7). For optically thick clouds with unknown cloud surface orientation, this introduces the ambiguity to be dealt with into the relation between $L_{0.87}$, $L_{2.10}$ and cloud optical properties. For the oblique viewing geometry, radiances for $r_{\mathrm{eff}} = 9\,\mu\mathrm{m}$ within the upper branch of the bow structure coincide
20 with radiance values for $r_{\mathrm{eff}} = 7\,\mu\mathrm{m}$. Nevertheless, towards higher values of $L_{0.87}$ there remain unambiguous regions where radiance pairs $(L_{0.87}, L_{2.10})$ of different effective radii do not overlap (compare line for $r_{\mathrm{eff}} = 13\,\mu\mathrm{m}$ in Figure 7).

Atmospheric
Measurement
Techniques

Open Access

Discussions

EGU
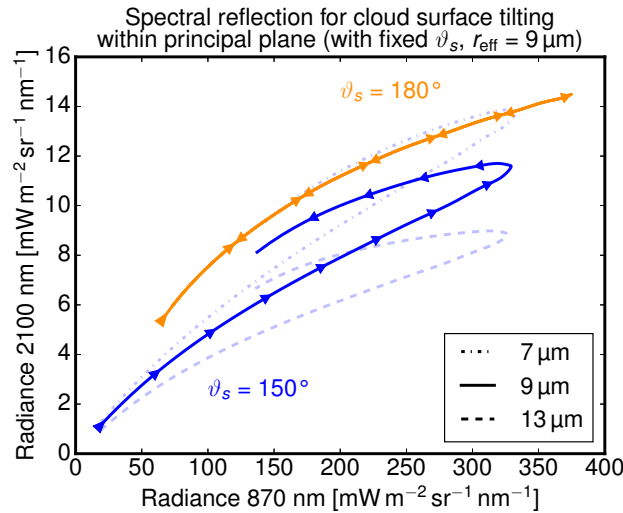
Figure 7. Spectral radiances used in 2-wavelengths retrievals at $\lambda = 870\,\text{nm}$ and $\lambda = 2100\,\text{nm}$ during the rotation of the cloud surface for observation geometries shown in Figure 7. Calculations of spectral reflection were done for an optically thick ($\tau = 500$) water cloud with a fixed effective radius $r_{\text{eff}} = 9\,\mu\text{m}$ with a fixed scattering angle of $\vartheta_s = 180°$ (orange line, $9\,\mu\text{m}$) and three different effective radii with a fixed scattering angle of $\vartheta_s = 150°$ (blue lines, $7\,\mu\text{m}$, $9\,\mu\text{m}$ and $13\,\mu\text{m}$).
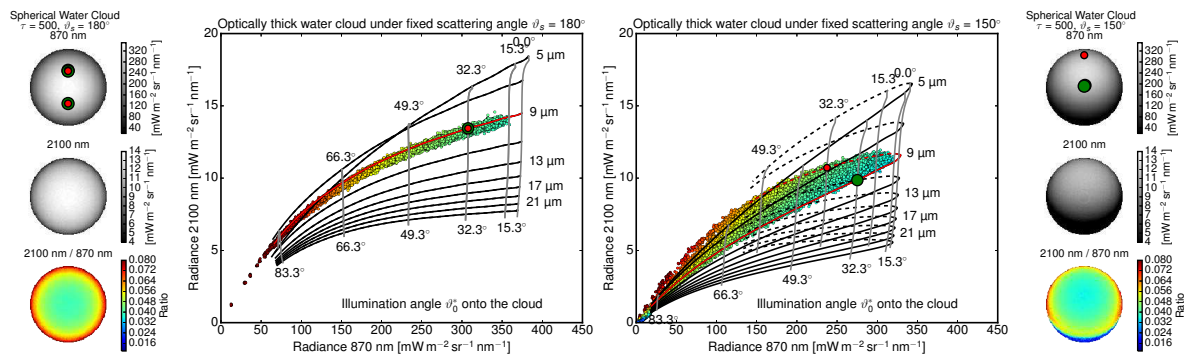
Figure 8. Spectral radiances at $\lambda = 870\,\text{nm}$ and $\lambda = 2.1\,\mu\text{m}$ for a spherical and optically thick water cloud with a with fixed $r_{\text{eff}} = 9\,\mu\text{m}$ observed at a fixed scattering angle of $\vartheta_s = 180°$ (left) and $\vartheta_s = 150°$ (right). Images of $L_{0.87}$, $L_{2.10}$ and their ratio are shown left and right to identify the origin of radiance pairs in the scatter plots. Radiances from one-dimensional DISORT simulations for optically thick water clouds with different effective radii are shown as black isolines. The gray isolines mark 1D radiance pairs with same local illumination angle ϑ_0^*.

4.1.1 3D

Next, the analysis is extended from principal plane considerations to a full 3D setup. To this end, 3D MYSTIC radiance simulations were done for a spherical, optically thick cloud and different scattering regimes of $\vartheta_s = 180°$ and $150°$. Figure Figure 8

Atmospheric
Measurement
Techniques
Discussions
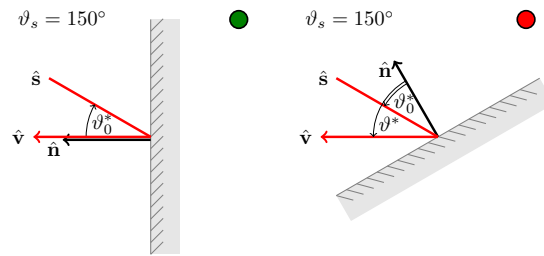

Figure 9. Two observation geometries with same scattering angle $\vartheta_s = 150°$ and same local illumination angle $\vartheta_0^* = 30°$. **(left)** Viewing direction perpendicular ($\vartheta^* = 0°$) to the cloud surface corresponding to the configuration found at the green dot in Figure 8 (right). **(right)** Oblique viewing perspective ($\vartheta^* = 60°$) corresponding to the configuration found at the red dot in Figure 8 (right).

shows the results in 2-wavelength diagrams (center) and as images for the direct backscatter direction (left) and for a scattering angle of 150° (right). In the 2-wavelength diagrams the radiance pairs ($L_{0.87}$, $L_{2.10}$) from the 3D radiative transfer forward simulation are shown as scattered points, the results from the one-dimensional DISORT simulations for different effective radii are shown as isolines. Within the principal plane, the large green and red dots indicate cloud surfaces with same local illumi-
5   nation angle $\vartheta_0^* = 30°$. Figure 9 illustrates the viewing and illumination setup at the green and red dot. In the following, the green dot will mark the cloud surface with smaller local viewing angle ($\vartheta^* < \vartheta_0^*$), the red dot the cloud surface with larger local viewing angle ($\vartheta^* > \vartheta_0^*$). In the 2-wavelength diagrams, the gray isolines mark radiance pairs with same local illumination angle ϑ_0^*. The corresponding images show radiances $L_{0.87}$, $L_{2.10}$ and the colored ratio $\frac{L_{2.10}}{L_{0.87}}$ to aid mapping radiance pairs with their spatial location.

10   This ratio reflects the radial symmetry of the local illumination angle for $\vartheta_s = 180°$ (Figure 8 left part). For this direct backscatter geometry in Figure 8, 3D results for $r_{eff} = 9\,\mu m$ match the 1D DISORT results for $r_{eff} = 9\,\mu m$ very closely. Due to the radial symmetry of the local illumination angles, radiance values also decrease radially symmetric with more oblique cloud surfaces. Albeit restricted to airborne or spaceborne platforms, this perspective minimizes the 3D effect on radiance ambiguities caused by unknown cloud surface orientations. The picture changes when the observer leaves the backscatter
15   geometry as shown for a scattering angle of $\vartheta_s = 150°$ in Figure 8 on the right. As already shown with the DISORT results in Figure 7, the radiance pairs form a bow-like pattern with higher $L_{2.10}$ values at more oblique surface orientations. Furthermore, the red and green dots with same local illumination angle now become separated since $\vartheta^* \neq \vartheta_0^*$. While radiance at the non-absorbing wavelength drops considerably with a more oblique local viewing angle ($\vartheta^* = 60°$, red dot), radiance at the absorbing wavelength changes only slightly at very steep local viewing angle ($\vartheta^* = 0°$, green dot). Consequently, droplets at the green
20   dot with $r_{eff} = 9\,\mu m$ could be miss-interpreted as effective radius $r_{eff} = 7\,\mu m$ or even $5\,\mu m$.

For a deeper insight into the different observation at the green and red dot, we analyze the angular distribution of cloud reflectance at the absorbing and non-absorbing wavelength. For a fixed illumination angle $\vartheta_0^* = 30°$, Figure 10 shows the DISORT radiances for different effective radii and all possible local viewing angles. The two locations considered in Figure 8
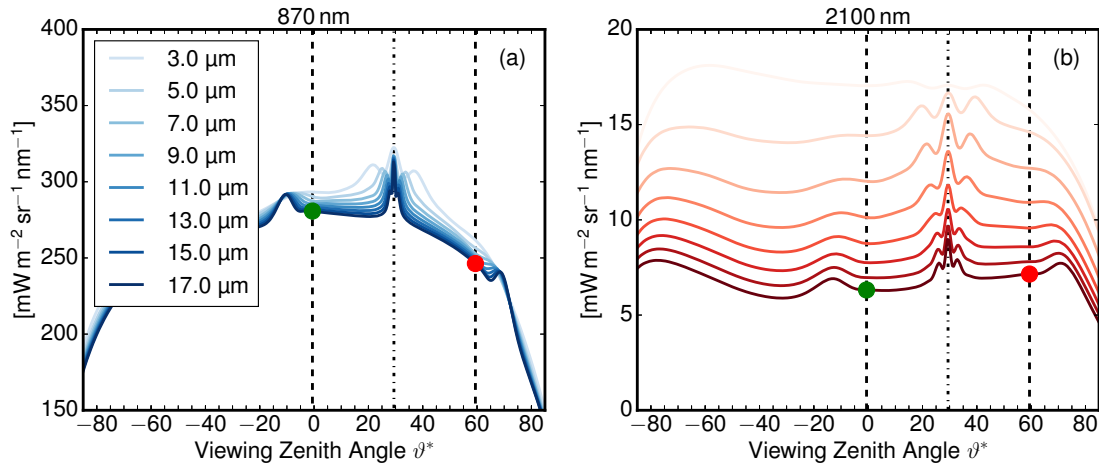
Figure 10. Spectral radiances at **(a)** $\lambda = 870\,\mathrm{nm}$ and **(b)** $\lambda = 2.1\,\mathrm{\mu m}$ for an optically thick water cloud for different effective radii as a function of relative viewing angle ϑ^* for a fixed illumination of $\vartheta_0^* = 30°$. The green and red dots mark viewing configurations shown in Figure 8 (right).

(right) are, again, marked with green and red dots. Obviously, the angular characteristic differs between the absorbing and non-absorbing wavelength. For a wide range of scattering angles $\vartheta_s < 180°$, the radiance at the absorbing wavelength remains quite constant between steep (green dot) and oblique (red dot) viewing perspective while the radiance at the non-absorbing wavelength is considerably smaller for the oblique viewing perspective. This asymmetric behavior becomes less pronounced

5 for scattering angles near $\vartheta_s = 180°$, when the red and green dots both move symmetrically towards the backscatter peak in Figure 10. The reason for this different angular reflectance is connected with different photon penetration depths at the two wavelengths. Smaller penetration depths lead to a more uniform reflection, while larger penetration depths lead to a stronger reflection perpendicular to the cloud surface.

Marshak et al. (2006a) and Zinner et al. (2008) do not investigate these reasons for the cloud geometry caused scatter

10 of reflected radiance in detail. Nonetheless, they suggest to limit the influence of missing geometry information by additional consideration of vertical thermal radiation temperature gradients (containing part of the geometry information). In the following a more systematic use of available geometry information in the visible, near-infrared spectrum itself is presented.

4.2 Additional information from surrounding pixels

Here a technique is presented that uses information from surrounding pixels to classify the geometrical environment of the

15 considered pixel. Already Varnai and Marshak (2003) discussed and developed a method to determine how the surrounding of a cloud pixel influences the pixel brightness. In a recent study, Okamura et al. (2017) also use surrounding pixel to train a neural network to retrieve cloud optical properties more reliably.

Atmospheric
Measurement
Techniques
Discussions
Open Access

As discussed in the preceding section, ambiguous radiances are mainly caused by the lower $L_{0.87}$ radiances from oblique cloud surfaces when compared to the more steeper cloud surfaces. With the sun behind the observer and convex cloud structures, cloud regions with steeper surfaces should generally be brighter than their surroundings while oblique surfaces should be darker than their surroundings. In line with recent developments of multi-pixel retrievals, the method should therefore deter-

5 mine if the pixel is surrounded by darker pixels or surrounded by brighter pixels. At the same time, the method should be robust regarding instrument or radiative Monte Carlo noise between adjacent pixels. To this end, a 2D Gaussian band-pass filter is used to classify different illumination regimes in simulated or measured radiance images. As a 2D band-pass filter, it compares the brightness of each pixel with the brightness of other pixels in the periphery. Pixels are classified according to their positive or negative radiance deviation compared to their surrounding pixels. The band-pass filter consists of two 2D Gaussian functions

10 $H_{\mathrm{LP}}(x,y)$ and $H_{\mathrm{HP}}(x,y)$ which specify the inner and outer search radius for this comparison. By neglecting directly adjacent pixels, the filter is insensitive to pixel-to-pixel noise of CMOS sensors or Monte Carlo radiative transfer calculations. With $D(x,y)$ as the distance (Equation (7)) from the origin pixel, D_H and D_L limit the inner and outer search radius respectively:

$$D(x,y) = \sqrt{x^2 + y^2} \tag{7}$$

$$H_{\mathrm{LP}}(x,y,D_L) = e^{\frac{-D(x,y)^2}{2D_L^2}} \tag{8}$$

15 $$H_{\mathrm{HP}}(x,y,D_H) = 1 - e^{\frac{-D(x,y)^2}{2D_H^2}} \tag{9}$$

Both functions $H_{\mathrm{LP}}(x,y)$ and $H_{\mathrm{HP}}(x,y)$ are then combined into the Gaussian Band-pass Kernel $H_{\mathrm{BP}}(x,y)$:

$$H_{\mathrm{BP}}(x,y,D_L,D_H) = H_{\mathrm{LP}}(x,y,D_L) * H_{\mathrm{HP}}(x,y,D_H) \tag{10}$$

$$g_{\mathrm{class}}(x,y,D_L,D_H) = \arctan H_{\mathrm{BP}}(x,y,D_L,D_H) \tag{11}$$

The absolute deviation values obtained from $H_{\mathrm{BP}}(x,y)$ can vary from scene to scene. For the classification into steep or oblique

20 perspectives, we are more interested in the relative deviation. To constrain the gradient classifier $g_{\mathrm{class}}(x,y)$ into a fixed interval, the arcus tangent function is used (Equation (11)).

To demonstrate the method, the cloud field illustrated in Figure 5 was used again for radiance calculations, but with a fixed effective radius of $r_{\mathrm{eff}} = 8\,\mu\mathrm{m}$. For this fixed effective radius, the broad radiance distribution of $L_{0.87}$ and $L_{2.10}$ shown in Figure 11a is mainly caused by the different cloud surface orientations discussed in the previous section. In order to identify

25 the regions leading to the upper part of the radiance scatter cloud in Figure 11a, an exponential function was fitted (black line) to the data points to determine the positive (blue) or negative (red) deviation $\Delta L_{2.10}$ from the typical best fit (black) line for each radiance pair.

In the following, this deviation $\Delta L_{2.10}$ is taken as a reference for a perfect separation of 3D radiance ambiguities. A method that would yield the same separation from observable parameters could be used as a proxy to mitigate the problem of ambiguous

30 radiances. For the gradient classifier g_{class}, a maximal correlation with $\Delta L_{2.10}$ is found when the band-pass operates between $D_H = 0.25°$ and $D_L = 1.5°$. This optimal search region was found by correlating the result from g_{class} with the deviation $\Delta L_{2.10}$ while the nearby and distant cut-off D_H and D_L was varied. For a cloud side at a distance of $6\,\mathrm{km}$, pixel within

Atmospheric
Measurement
Techniques
Discussions

EGU

Open Access
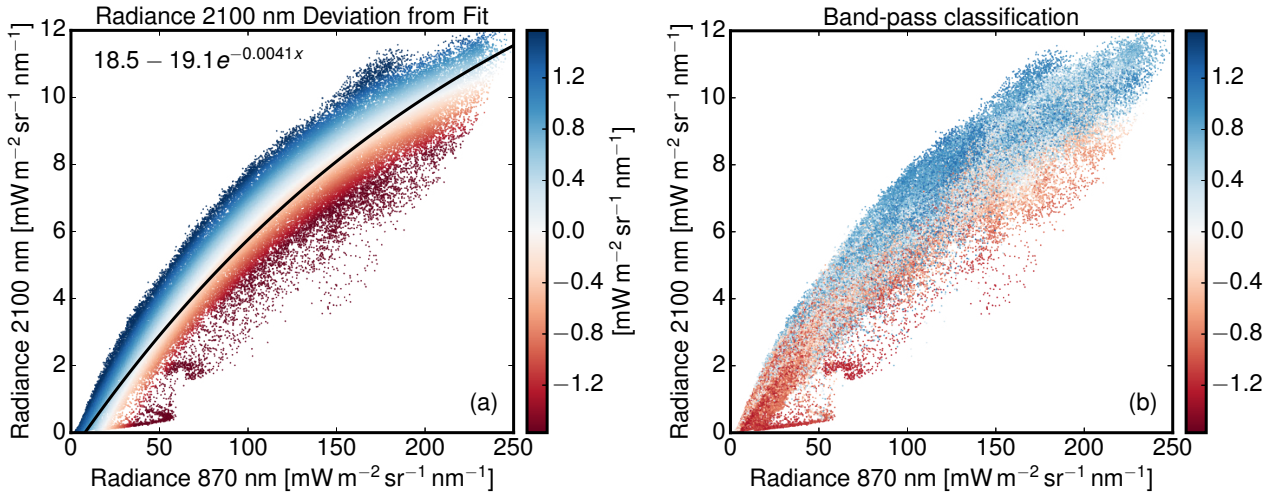
Figure 11. (a) 2-wavelength diagram for the MYSTIC calculation shown in Figure 5a but with a fixed effective radius of $r_{\text{eff}} = 8\,\mu\text{m}$. **(b)** Result of the gradient classifier g_{class} applied to the same scene.
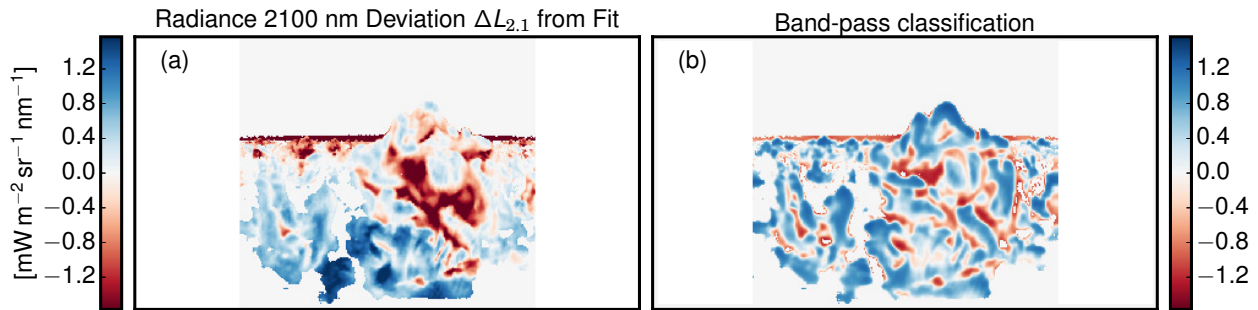
Figure 12. (a) Deviation $\Delta L_{2.10}$ from the fit in the 2-wavelength diagram in Figure 11a used as a reference for the **(b)** gradient classifier g_{class} which puts the pixel radiance into context with surrounding pixels.

a search region of $30\,\text{m}$ to $150\,\text{m}$ around the pixel would be considered. Figure 11b shows the separation provided by the gradient classifier (Equation (11)). Reference and proxy are also shown as images in Figure 12, where the deviation $\Delta L_{2.10}$ from the fit in the scatter plot is shown as reference on the left (Figure 12a) and the result of the gradient classifier on the right (Figure 12b).

Apparently, the gradient classifier g_{class} is able to reproduce the general appearance of the gradient classifier g_{class} used in Figure 12. It is able to separate the radiance distribution into positive and negative radiance deviations $\Delta L_{2.10}$ at high as well as at low radiance values. Large g_{class} values are more likely to be associated with a steeper illumination angle compared to the viewing angle, while smaller values are more likely to be associated with a more oblique illumination angle compared to the viewing angle. For two pixels with same illumination angle, $g_{\text{class}} > 0$ therefore marks the upper *radiance branch* in Figure 7 for $\vartheta_s = 150°$, while $g_{\text{class}} < 0$ marks the lower *radiance branch*. Based on this feature, the band-pass classification g_{class} can

Atmospheric
Measurement
Techniques
Discussions

Open Access
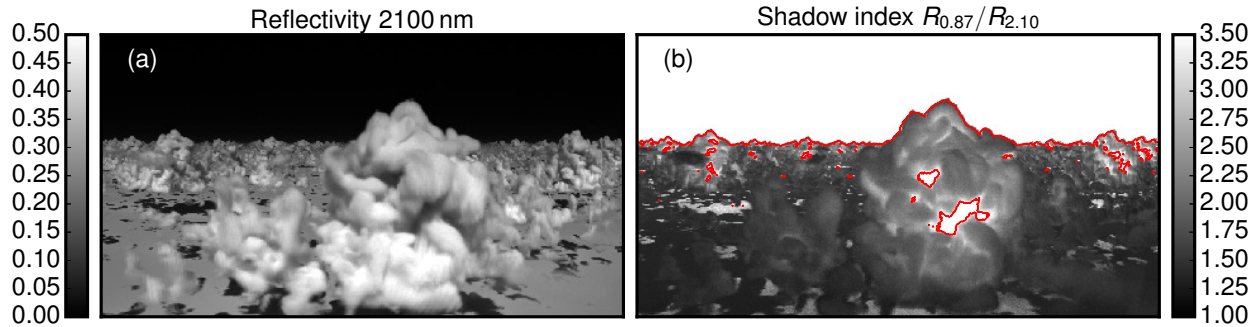
Figure 13. (a) Reflectivity at $2.1\,\mu\mathrm{m}$ for the cloud scene shown in Figure 5 **(b)** Shadow index $R_{0.87}/R_{2.10}$ highlighting regions of enhanced cloud absorption caused by multiple diffuse reflections.

be used as a proxy to determine the location of a pixel within the radiance distribution. In the following, the gradient classifier g_{class} is used for the 3D forward calculation ensemble as well as for real measurements.

4.3 Exclusion of cloud shadows

Depending on the illumination, cloud surfaces can also be in direct shadow if the local solar zenith angle onto the cloud surface 5 ϑ'_0 is larger than $90°$. Illuminated cloud parts can also cast shadows onto other cloud parts. Without direct illumination, reflected photons from these parts originate from previous scattering events and are affected by those. For this reason, shadowed cloud parts have to be filtered out before applying any retrieval based on direct illumination.

Usually radiation from shadow regions encountered more absorption compared to directly reflected light (Vant-Hull et al., 2007). This enhanced absorption is visible in Figure 13, where the reflectivity at $2.1\,\mu\mathrm{m}$ drops considerable (Figure 13a). As a 10 proxy of enhanced absorption, the reflectivity ratio $R_{0.87}/R_{2.10}$ (Figure 13b) increases in this region. In the following, this ratio will be used as *shadow index* f_{shad} to exclude pixel for which light has likely undergone multiple diffuse reflections:

$$f_{\mathrm{shad}} = \frac{R_{0.87}}{R_{2.10}} > 3.5 \qquad \text{(shadowed)} \tag{12}$$

The manual inspection of many scenes confirmed $f_{\mathrm{shad}} > 3.5$ as viable threshold for most shadowed cloud regions. In addition, a threshold of $L_{0.87} > 75 \left[\mathrm{mWm}^{-2}\mathrm{nm}^{-1}\mathrm{sr}^{-1} \right]$ is used to focus the retrieval on optically thicker clouds and to filter out clear-15 sky regions.

5 Retrieval

In this section, the Monte Carlo sampled posterior distributions $p(r_{\mathrm{eff}}|L_{0.87}, L_{2.10})$ will be used to infer droplet size profiles from convective cloud sides. As mentioned in Section 2.2, the posterior $p(r_{\mathrm{eff}}|L_{0.87}, L_{2.10})$ can be derived from Bayes' theorem by solving the easier forward problem $p(L_{0.87}, L_{2.10}|r_{\mathrm{eff}})$ for all values of r_{eff}.
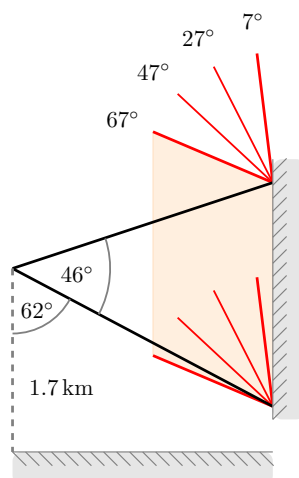
Figure 14. Setup of the viewing geometry ($\Delta\vartheta = 46°$, starting $62°$ from nadir) and the illumination geometry ($\vartheta_0 = 7, 27, 47$ and $67°$) for the airborne ($h = 1.7\,\mathrm{km}$) 3D forward simulation ensemble. The horizontal extent of the field of view is $\Delta\varphi = \pm45°$ from the principal plane.

The three-dimensional radiative transfer code MYSTIC is applied to LES model clouds to obtain simulations of realistic *specMACS* measurements. A whole ensemble of these MYSTIC forward simulations of cloud sides will then be incorporated within the statistical framework introduced in Section 2.1. Subsequently, the sampled statistics of reflected radiances are analyzed for their sensitivity to the effective cloud droplet radius.

5.1 Implementation of the 3D forward radiative transfer ensemble

In the following, an ensemble of 3D radiative transfer simulations is created to sample the posterior probability distribution $p(r_{\mathrm{eff}}|L_{0.87}, L_{2.10})$. The ensemble of simulated cloud side measurements is set up by using the method to select suitable observation perspectives introduced in Section 3.1. During the radiative transfer calculations, the MYSTIC REFF method (Section 3.1) determines the apparent effective radius which links the simulated radiances with the corresponding cloud droplet sizes. Despite the variance reduction methods in the MYSTIC code itself (Buras and Mayer, 2011), the time-consuming 3D technique still limits the number of model runs. Figure 14 illustrates the different illumination setups and the viewing geometry included within the 3D forward simulation ensemble. With LES cloud tops between 1.5 and $2.0\,\mathrm{km}$, the airborne perspective is set to an altitude of $h = 1.7\,\mathrm{km}$. Since the retrieval should also be applicable in tropical regions, solar zenith angles were chosen at $\vartheta_0 = 7, 27, 47$ and $67°$.

For each observation position selected in Section 3.1, images of cloud sides were simulated using MYSTIC. In line with the position selection method, the field of view of each image has an azimuthal opening angle of $\Delta\varphi = \pm45°$, a zenithal opening angle of $\Delta\vartheta = 46°$ and is centered around $5°$ below the horizon. Comprising 720×368 pixel, each image was calculated with a

spatial resolution of $0.125°$. For this image setup, solar radiances were calculated at the non-absorbing wavelength $\lambda = 870\,\text{nm}$ ($L_{0.87}$) and the absorbing wavelength $\lambda = 2100\,\text{nm}$ ($L_{2.1}$). Since the width of the cloud droplet size distribution has no large impact on radiances at $L_{0.87}$ and $L_{2.1}$ (analysis not shown), the scattering properties were derived according to Mie theory using modified gamma size distributions with a fixed width of $\alpha = 7$ and the effective radius as simulated by RAMS. For the

5   ensemble, the surface albedo was set to zero since the influence of radiation reflected by vegetation on the ground is masked out in measurements. This technique will be described in the following part 2 paper.

Atmospheric aerosol was included by using the continental average mixture from the Optical Properties of Aerosols and Clouds (OPAC) package (Hess et al., 1998). The aerosol optical thickness (AOT) at $550\,\text{nm}$ is around $\tau_a^{550} = 0.15$ for this profile. This aerosol profile is typical for anthropogenically influenced continental areas and contains soot and an increased

10   amount of insoluble (e.g. soil) as well as water-soluble (e.g. sulfates, nitrates and organic) components.

A compromise had to be found to minimize the noise of the 3D Monte Carlo radiative transfer results and to keep computation time within reasonable limits. Here, the Monte Carlo noise should stay below the accuracy of the radiometric sensor which is assumed to be $\sim 5\%$. The photon number was thus chosen to be 2000 photons per pixel which leads to a standard deviation of about 2%.

15   All 12 RICO LES snapshots between $12\,\text{h}\,00\,\text{min}$ LT (local time) and $14\,\text{h}\,00\,\text{min}$ LT with a time step of $10\,\text{min}$ were included in the 3D forward simulation ensemble. For four azimuth directions $\varphi = 45°$, $135°$, $225°$ and $315°$, suitable locations for cloud side observations were determined in each LES snapshot. In summary, for each ensemble $12 \times 4 = 48$ cloud scenes have been simulated for 4 solar zenith angles and 2 wavelengths with 720×368 pixel, totaling $101,744,640$ forward simulation pixels. In total, 2.0×10^{11} photons have been traced on a computing cluster with 300 cores consuming $2.0 \times 10^8\,\text{s}$ of CPU time.

20   **5.2   Construction of the lookup table**

In the next step, simulated radiances were binned into a multidimensional histogram with equidistant steps in $L_{0.87}$, $L_{2.10}$, r_{eff}, ϑ and g_{class}. Table 1 shows the range and step sizes of this histogram. During this discretization, radiances were counted in adjoining bins by linear interpolation. In the following, the histogram will be normalized to yield the posterior probability $p(r_{\text{eff}} | L_{0.87}, L_{2.10})$.

25   **5.3   Biased and unbiased priors**

In our input cloud field, the effective radius always increases with height which might impact the retrieval. The retrieval should not exhibit any trend towards a specific profile. Instead of an unbiased result, the retrieval would otherwise only reflect a-priori knowledge about the vertical profile of cloud microphysics. For this reason, the assumed prior is a key element to be considered in the sampling of the posterior and the subsequent Bayesian inference. In the case of cloud side remote sensing, two possible

30   priors $p_{\text{pr}}(r_{\text{eff}})$ come into mind: a uniform prior or the LES model provided prior. For the LES model the prior is a function of viewing geometry, as some r_{eff} are more likely to be observed under certain viewing directions. In particular, relative frequency of r_{eff} for different scattering angles ϑ_s and gradient classes should be the same. For this problem, the prior probability should be uniform in r_{eff} to avoid the introduction of any bias.

Atmospheric
Measurement
Techniques
Discussions

Open Access

EGU

Table 1. Variables, range and step size into which simulated radiances are binned to obtain a multidimensional histogram which is then used as a lookup table.

Variable	Range		Step	Bins
	Lower	Upper		
$L_{0.87}^{*}$	0	290	5	58
$L_{2.1}^{*}$	0	18	0.2	90
$r_{\text{eff}}^{\dagger}$	3	25	2	11
ϑ	$80°$	$180°$	$10°$	10
g_{class}	$-\frac{\pi}{2}$	$+\frac{\pi}{2}$	$\frac{\pi}{5}$	5

$*\text{mW m}^{-2}\text{nm}^{-1}\text{sr}^{-1}$, $\dagger\mu\text{m}$

Another important prerequisite of the Monte Carlo based Bayesian approach is the sufficient sampling of the likelihood probability $p(L_{0.87}, L_{2.10}, r_{\text{eff}})$. Naturally, effective radii not included in the ensemble of forward calculations cannot be retrieved using Bayesian inference. Furthermore, it should be kept in mind that sparsely sampled likelihood regions are probably not representative for the whole distribution. This is especially true for the smallest and largest effective radii contained in the

5   LES model.

For this reasons an unbiased coverage of the likelihood probability is pursued. In order to meet this objective, the ensemble with the *normal* cloud microphysics data from the LES model was complemented with calculations with vertically *flipped* cloud microphysics. The flipped cloud microphysics are derived by subtracting the original effective radius value $r_{\text{eff}}^{\text{orig}}$ from $16\,\mu\text{m}$ for the polluted cloud ensemble ($\text{CCN} = 1000\,\text{cm}^{-1}$) and from $26\,\mu\text{m}$ for the clean cloud ensemble ($\text{CCN} = 100\,\text{cm}^{-1}$):

$$r_{\text{eff}}^{\text{flip}} = 16\,\mu\text{m} - r_{\text{eff}}^{\text{orig}} \qquad (\text{CCN} = 1000\,\text{cm}^{-1}) \tag{13}$$

10

$$r_{\text{eff}}^{\text{flip}} = 26\,\mu\text{m} - r_{\text{eff}}^{\text{orig}} \qquad (\text{CCN} = 100\,\text{cm}^{-1}) \tag{14}$$

These values are chosen to be at least $4\,\mu\text{m}$ larger than the maximum values found in the respective ensembles to ensure positive and realistic values for $r_{\text{eff}}^{\text{flip}}$. In order to preserve the optical thickness τ^{orig} of the original cloud field (Equation (16)), the original liquid water content LWC^{orig} is changed (Equation (17)) according to the well established relationship (Equation (15)) in the

15   optical limit:

$$\tau \propto \frac{\text{LWC}}{r_{\text{eff}}} \tag{15}$$

$$\tau^{\text{flip}} \equiv \tau^{\text{orig}} \tag{16}$$

$$\text{LWC}^{\text{flip}} = \frac{r_{\text{eff}}^{\text{flip}}}{r_{\text{eff}}^{\text{orig}}} \text{LWC}^{\text{orig}} \tag{17}$$
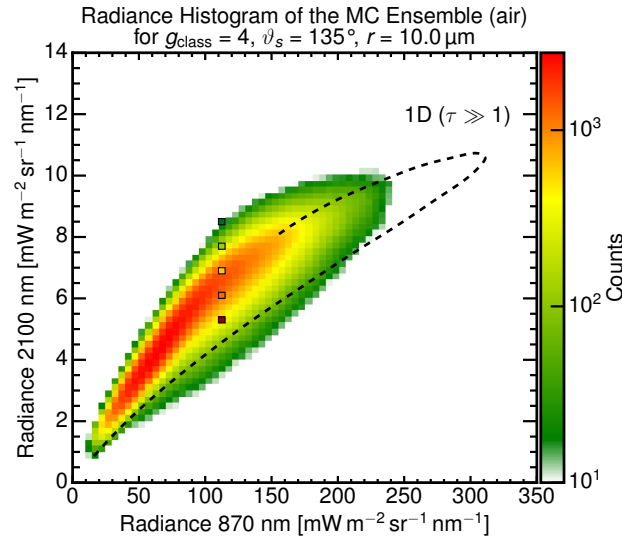
Figure 15. Radiance histogram ($\vartheta_s = 135°$, $g_{\text{class}} = 4$) the 3D forward simulation ensemble of cloud sides which illustrates the radiance spread for the effective radius bin of **(top)** $r_{\text{eff}} = 10\,\mu\text{m}$. The dashed line shows reflected radiances which were calculated with DISORT (1D RT code) for an optically thick ($\tau = 500$) water cloud with the same effective radius and the same scattering angle for different cloud surface inclinations within the principal plane. The colored dots indicate locations within the histogram for which the posterior distributions are shown in Figure 16.

5.4 Radiance and posterior distributions

The following section will present the radiance histograms $n(L_{0.87}, L_{2.10}, r_{\text{eff}})$ and the corresponding posterior distributions $p(r_{\text{eff}} | L_{0.87}, L_{2.10})$. Analogous to the likelihood distribution, the first gives the spread of radiances for a given effective radius r_{eff}, while the latter describes the spread of effective radii r_{eff} for a given radiance pair $L_{0.87}$ and $L_{2.10}$. Figure 15 shows a 2D

5 histogram of simulated radiance combinations $L_{0.87}$ and $L_{2.10}$ for the airborne perspective. The histogram shows the results for the effective radius bin centered at $r_{\text{eff}} = 10\,\mu\text{m}$, the scattering angle bin between $\vartheta_s = 130°$ and $140°$ and the gradient class bin $g_{\text{class}} = 4$ which holds pixels that are brighter as their surroundings. The spread of the radiance from three-dimensional cloud sides, for the most part, can be explained by the one-dimensional DISORT results (dashed line for variable cloud surface inclination).

10 After normalization of the histograms in Equation (3) and after the application of the uniform prior in Equation (4), the posterior probabilities $p(r_{\text{eff}} | L_{0.87}, L_{2.10})$ can be examined. Figure 16 shows posterior probabilities as a function of r_{eff} for different radiances $L_{2.10}$ at the absorbing wavelength corresponding to the colored dots in the histogram panels (Figure 15). The vertical lines indicate the corresponding mean effective radius for each posterior distribution which were derived using Equation (18). The descending order of mean effective radii with ascending radiance $L_{2.10}$ demonstrates the general feasibility

15 to discriminate different effective radii in cloud side measurements. Albeit the relatively large spread in r_{eff}, the measurement

Atmospheric
Measurement
Techniques
Discussions

Open Access

EGU
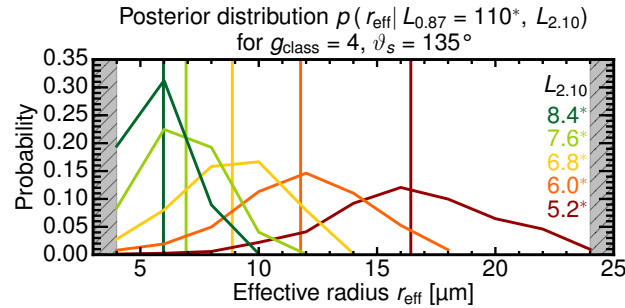
Figure 16. (left) Posterior probability ($\vartheta_s = 135°$, $g_{\mathrm{class}} = 4$) for the airborne 3D forward simulation ensemble for a fixed radiance $L_{0.87} = 110\,\mathrm{mWm^{-2}nm^{-1}sr^{-1}}$ at the non-absorbing wavelength and different $L_{2.10}$ radiances at the absorbing wavelength. The vertical lines indicate the corresponding mean effective radius for each posterior distribution. The color of the different posterior distributions corresponds with the dots in the radiance histograms in Figure 15.

of a radiance pair ($L_{0.87}$, $L_{2.10}$) can still narrow down r_{eff} to $\pm1.5\,\mu\mathrm{m}$ around the most likely value. In the following, the tabulated set of posterior distributions is used as lookup table for the effective radius retrieval.

5.5 Bayesian inference of the effective radius

Based on this lookup table of posterior probabilities $p(r_{\mathrm{eff}}|L_{0.87}, L_{2.10})$, the actual retrieval of effective radii can now be

5 introduced. After a set of spectral radiance pairs $L_{0.87}$ and $L_{2.10}$ has been measured, the band-pass filter (Section 4.2) is applied to the $L_{2.10}$ image to derive the gradient classifier g_{class}. Scattering angles are calculated from the orientation and navigation data of the aircraft. With the four parameters, $L_{0.87}$, $L_{2.10}$, g_{class} and ϑ_s defined for each pixel, the corresponding posterior is retrieved from the lookup table by linear interpolation between posteriors defined at the bin centers of the lookup table. Finally, the mean effective radius $\langle r_{\mathrm{eff}}\rangle$ and the corresponding standard deviation $\sigma(r_{\mathrm{eff}})$ can be derived as first and

10 second moments of the posterior distribution:

$$\langle r_{\mathrm{eff}}\rangle = \int r_{\mathrm{eff}}\, p(r_{\mathrm{eff}}|L_{0.87}, L_{2.10})\, dr_{\mathrm{eff}}. \tag{18}$$

$$\sigma(r_{\mathrm{eff}}) = \sqrt{\int \left(r_{\mathrm{eff}} - \langle r_{\mathrm{eff}}\rangle\right)^2 p(r_{\mathrm{eff}}|L_{0.87}, L_{2.10})\, dr_{\mathrm{eff}}}. \tag{19}$$

This 1-sigma standard deviation $\sigma(r_{\mathrm{eff}})$ will be referred to as the *statistical retrieval uncertainty*.

6 Numerical analysis of the retrieval

15 The next section will examine the stability of the statistical relationship between reflected radiance and cloud droplet size. How well can we retrieve the cloud droplet size after different viewing directions and cloud surface orientations have been combined within one lookup table? To answer this, the statistical retrieval is applied to simulated cloud side measurements

for which the underlying effective radius is known. First, this is done for scenes that have already been included in the lookup table. Using scenes with normal and flipped effective radius profile, the lookup table is tested for an inherent bias towards a specific effective radius profile that could be caused by the chosen forward sampling strategy. In addition, tests are repeated for the same scenes with a fixed effective radius of $8\,\mu\mathrm{m}$; a case which is not included in the lookup table.

5   6.1   Analysis of the sampling bias

By design the retrieval should not exhibit any trend towards a specific profile. The polluted scene ($N_{\mathrm{CCN}} = 1000\,\mathrm{cm}^{-1}$), already introduced in Figure 5a, will be used as a first case study. Figure 17 shows result of the statistical effective radius retrieval with the normal effective radius profile on top, the flipped profile in the center and a fixed effective radius profile at the bottom,. The retrieved mean effective radius is shown in the right panels (Figure 17c,f,i), the apparent effective radius $\langle r_{\mathrm{eff}}\rangle_{mc}$

10   ("the truth") is shown in the left panels (Figure 17a,d,g). The center panels compare the mean vertical profile (lines) and its spatial standard deviation (shaded areas) of the apparent (black) and the retrieved (green) effective radius. Furthermore, the green error bars show the error estimate $\sigma(r_{\mathrm{eff}})$ provided by the retrieval.

Overall, the retrieval reproduces all three profiles quite well. However, there are also large differences (up to $\pm 3\,\mu\mathrm{m}$) for specific cloud regions. For the normal profile as well as for the flipped profile, the retrieved effective radius agrees well with its

15   true value for the upper half of the cloud side. In the lower half of the cloud side near cloud base, the retrieval underestimates the large droplets of the flipped profile by up to $1\,\mu\mathrm{m}$.

Altogether, the statistical relationship between reflected radiance and cloud droplet size seems stable enough to be used for highly complex cloud sides. Moreover, these first results indicate that the retrieval seems to be resilient to the unrealistic, flipped cloud profiles included in its lookup table. Although the retrieval showed minor problems to retrieve the flipped profile,

20   no substantial bias towards a specific effective radius profile could be detected. Mean values for all heights agree within the natural variability in the LES data; the retrieval error estimate $\sigma(r_{\mathrm{eff}})$ seems to overestimate the uncertainty. Since these results were only obtained for a single cloud side scene, the following section will investigate these findings for a representative number of scenes.

Statistic stability for included scenes

25   In a first step, the retrieval will be tested for perspectives which are already included in the lookup table. This is done to test the retrieval for biases and to obtain a robust measure of correlation between the retrieval and the cloud side scenes it is composed of. By comparing this correlation with the correlation for cloud side scenes that are not included in the lookup table, this analysis will also be used to detect a potential over-fitting. There is the risk that the lookup table only reflects 3D effects that are specific for the included cloud side scenes.

30   In total, 9 cloud side perspectives were randomly chosen from the polluted as well as the clean dataset. For each perspective, the normal, the flipped as well as the fixed effective radius profile were tested. This amounts to $2 \times 9 \times 3 = 54$ test cases. For this statistical comparison, only reliable results with a retrieval error estimate $\sigma(r_{\mathrm{eff}})$ of less than $2.5\,\mu\mathrm{m}$ were included.
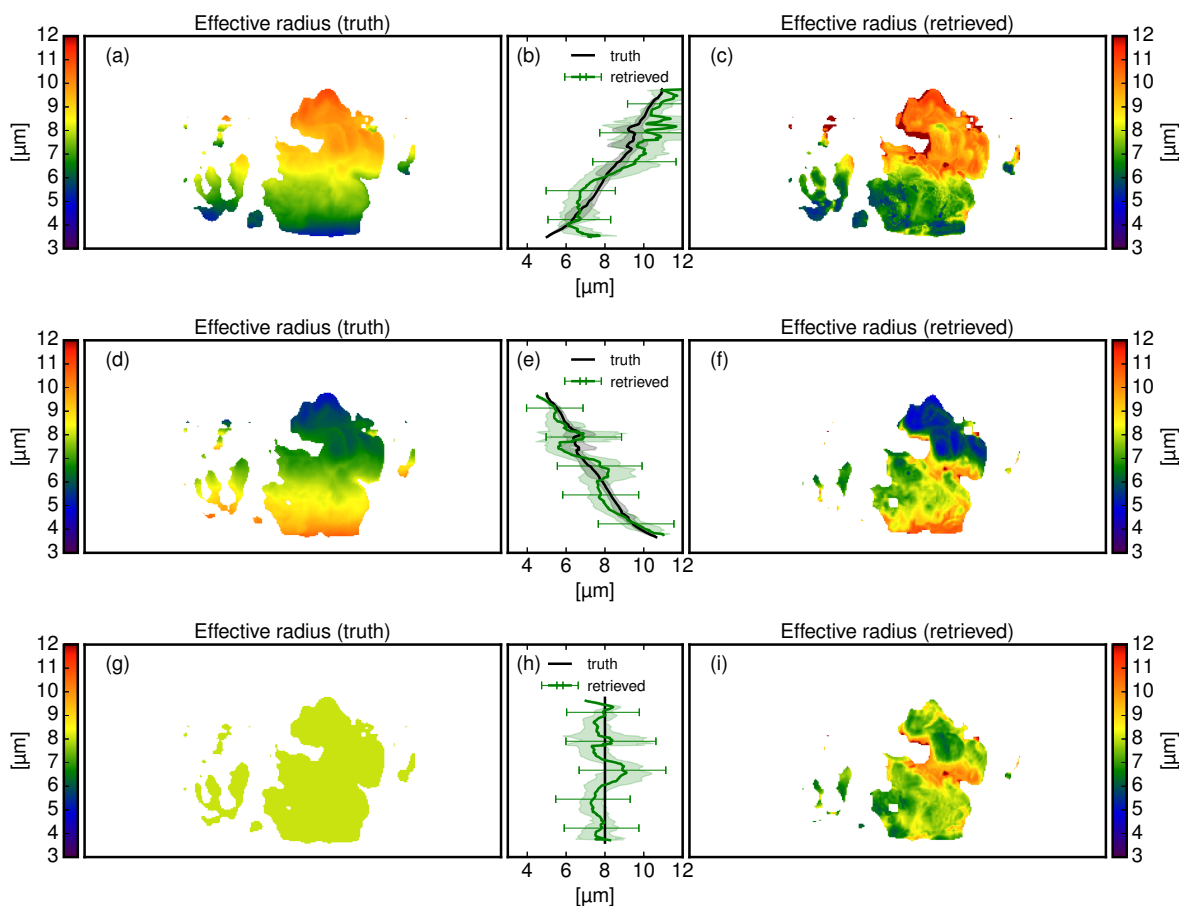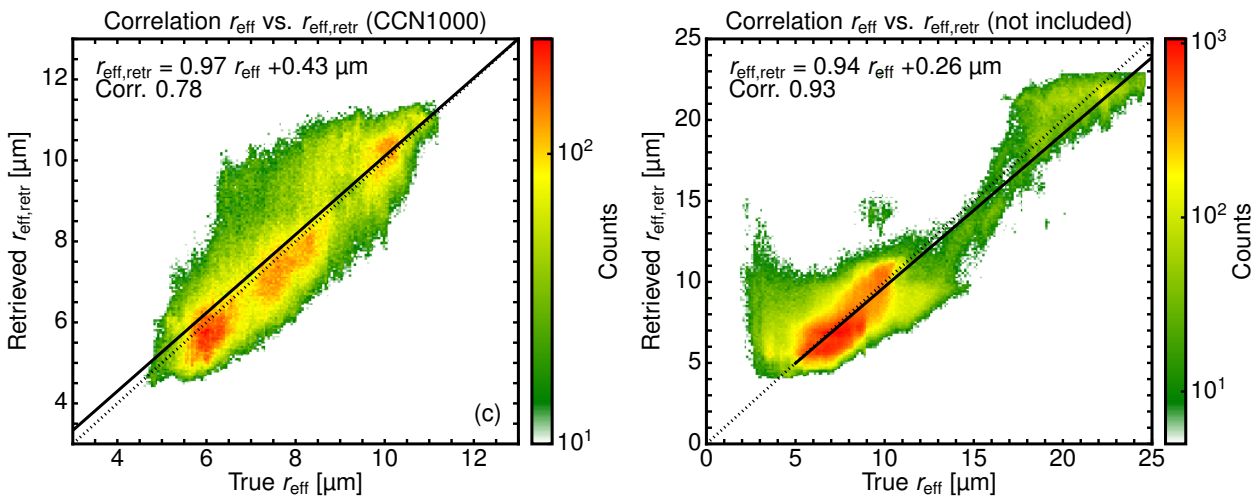
Figure 17. Retrieval test between the true effective radius (left) and the retrieved mean effective radius (right) for the normal (top), flipped (center) and fixed (bottom) effective radius profile. **(a)** Apparent effective radius $\langle r_{\mathrm{eff}} \rangle_{mc}$ for the normal profile, **(b)** Mean and standard deviation of the true (black) and retrieved (green) vertical effective radius profile (normal), **(c)** Retrieved mean effective radius for the normal profile, **(d)** Apparent effective radius $\langle r_{\mathrm{eff}} \rangle_{mc}$ for the flipped profile, **(e)** Mean and standard deviation of the true (black) and retrieved (green) vertical effective radius profile (flipped), **(f)** Retrieved mean effective radius for the flipped profile, **(g)** Apparent effective radius $\langle r_{\mathrm{eff}} \rangle_{mc}$ for the fixed profile, **(h)** Mean and standard deviation of the true (black) and retrieved (green) vertical effective radius profile (fixed), **(i)** Retrieved mean effective radius for the fixed profile

Figure 19a shows the correlation for the normal and the flipped polluted profiles which include around $358,000$ pixel. The linear regression with a slope of 0.97 and an offset of $0.43 \, \mu m$ shows no significant retrieval bias for these cases. The correlation between the true and the retrieved values is 0.78. A deeper insight can be gained through Table 2, where all comparisons are summarized separately for normal and flipped profiles. The higher correlation coefficient (0.80 vs. 0.73) seem to indicate a
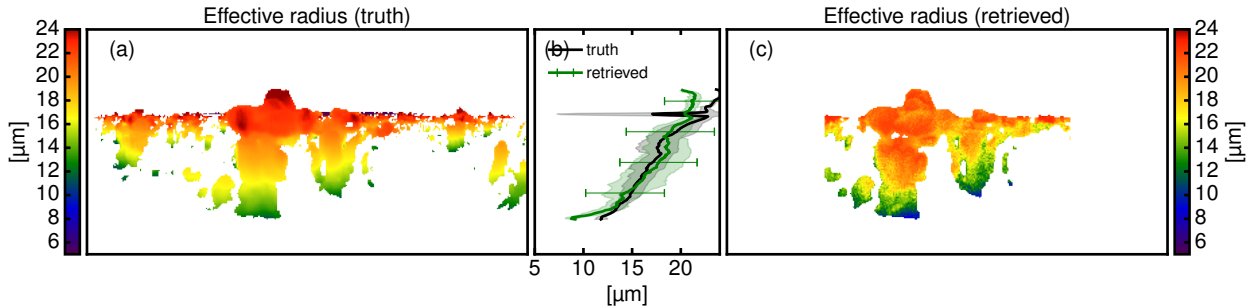
Figure 18. Retrieval comparison between the true effective radius (left) and the retrieved mean effective radius (right) for a cloud scene that was not included in the forward ensemble, **(d)** Apparent effective radius $\langle r_{\text{eff}} \rangle_{mc}$ for the airborne perspective, **(e)** Mean and standard deviation of the true (black) and retrieved (green) vertical effective radius profile, **(f)** Retrieved mean effective radius for the airborne perspective.


Figure 19. 2D histograms and linear regressions to determine the correlation between the true effective radius r_{eff} and the retrieved effective radius $r_{\text{eff,retr}}$ for **(a)** the included polluted cases ($N_{\text{CCN}} = 100\,\text{cm}^{-1}$) with normal and flipped effective radius profile and **(b)** for the not included cases with normal and flipped effective radius profile.

slightly better ability to detect the cases with a normal effective radius profile. Nevertheless, comparable linear regressions show no substantial bias towards the normal or the flipped cases. This confirms the observation made in the case study shown in Figure 17.

For the fixed effective radius profiles, the histogram in Figure 20 shows the deviation of the statistical retrieval with two
5 distinct modes. With most likely values between $0\,\mu\text{m}$ and $-1\,\mu\text{m}$, the retrieval underestimates the effective radius slightly. A second mode is found where the retrieval overestimates r_{eff} with values between $1\,\mu\text{m}$ and $2\,\mu\text{m}$. In combination, there is
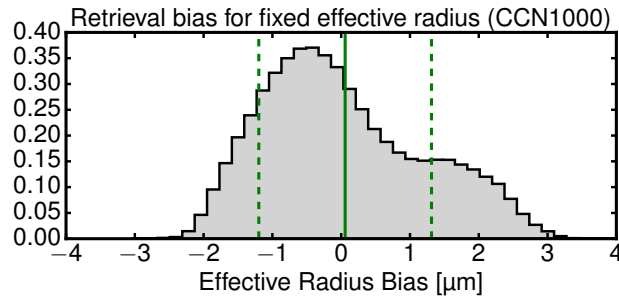
Figure 20. Retrieval deviations (retrieved $r_{eff,retr}$ - true r_{eff}) for the 9 cloud sides with fixed effective radius profile which are not included in the ensemble. The green line shows the average bias in retrieved effective radius $r_{eff,retr}$, the green dashed lines the root mean square error for $r_{eff,retr}$.

only a slight overestimation of $0.10\,\mu m$ with a larger standard deviation of $1.17\,\mu m$. A further investigation showed that the overestimation peak is connected with and found around undetected cloud shadows.

Statistic stability for unknown scenes

To check the retrieval for potential over-fitting, the retrieval was applied to unknown cloud side scenes. Nine new cloud side
5   perspectives were selected from the polluted and the clean LES runs. While the forward ensemble contains viewing azimuths of $45°$, $135°$, $225°$ and $315°$, these new cloud side perspectives were chosen for new viewing azimuths of $0°$, $90°$, $180°$ and $270°$ and only normal effective radius profiles were used this time.

Figure 18 shows one of these new cloud side scenes with a normal effective radius profile. In contrast to Figure 17, this clean ($N_{CCN} = 100\,cm^{-1}$) scene features a much larger range of cloud droplet sizes. Again, the statistical retrieval detects the
10 effective radius profile well. The true values for r_{eff} remain within the retrieval error estimate $\sigma(r_{eff})$. The comparison for all not included cloud sides is shown in Figure 19b. The correlation for the not included cases is 0.93, where around $339,000$ pixel are compared in total.

With nearly the same correlation coefficient, the retrieval performance remains the same when faced with unknown cloud side scenes. It can therefore be concluded that the retrieval is not trained only for the included cloud side scenes. Rather, it
15 represents the statistical relationship between reflected radiance and cloud droplet size for this cloud ensemble.

7   Conclusions

The presented work advanced a framework for the remote sensing of cloud droplet effective radius profiles from cloud sides which was introduced by Marshak et al. (2006a); Zinner et al. (2008) and Martins et al. (2011). Testing the feasibility of the approach, understanding its limitations and advancing its technique were central motivations of this work. Following scientific
20 objectives were addressed: (1) The degree of ambiguity of reflected radiances from cloud sides with respect to cloud droplet

Atmospheric
Measurement
Techniques
Discussions

Table 2. Results of retrieval performance tests when faced with normal, flipped and not included effective radius profiles, grouped for $CCN = 1000$, $CCN = 100$ and for all not included cases. Linear regression, bias, RMSE and correlation are calculated between true and retrieved effective radius.

Dataset	Slope	Offset	Bias	RMSE	Correlation
		CCN 1000			
Included Profiles	+0.93	+0.65	-0.18	+1.18	+0.81
- Normal Profiles	+0.95	+0.49	-0.12	+1.20	+0.80
- Flipped Profiles	+0.96	+0.52	-0.24	+1.17	+0.73
Unknown Profiles	+1.08	-0.85	+0.10	+1.26	+0.79
		CCN 100			
Included Profiles	+0.95	+0.19	-0.16	+2.17	+0.95
Unknown Profiles	+1.05	+0.25	-0.26	+2.28	+0.78
		All			
Unknown Profiles	+0.94	+0.26	-0.01	+1.86	+0.93

size was analyzed in the context of a unknown cloud geometry. (2) In this course, 3D radiative effects caused by the unknown cloud surface orientation were investigated. A technique was proposed to mitigate their impact on cloud droplet size retrievals by putting pixel in context with their surrounding. (3) Finally, an effective radius retrieval for the cloud side perspective was developed and tested for cloud scenes which were used during the retrieval development as well as for unknown scenes. The

5 scope of this work was limited to the liquid part of convective liquid water clouds, e.g. Cumulus and Cumulus congestus, which exhibit well-developed cloud sides. In principle, the proposed technique could also be extended to ice clouds.

In a first step, this work introduced a statistical framework for the proposed remote sensing of cloud sides following Marshak et al. (2006a). A statistical relationship between reflected sunlight in a near-visible and near-infrared wavelength and droplet size is found following the classical approach by (Nakajima and King, 1990). By simulating the three-dimensional radiative

10 transfer for high-resolution LES model clouds using the 3D radiative transfer model MYSTIC (Monte Carlo code for the physically correct tracing of photons in cloudy atmospheres), probability distributions for this relationship were sampled. These distributions describe the probability to find a specific droplet size after a specific solar reflectance pair of values has been measured. In contrast to many other effective radius retrievals, this work thereby provides essential information about the retrieval uncertainties which are intrinsically linked with the reflectance ambiguities caused by three-dimensional radiative

15 effects. Furthermore, this work developed a technique (Section 4.2) to reduce 3D radiance ambiguities when no information about the cloud surface orientation is available. More precisely, additional information from surrounding pixels was used to classify the environment of the considered pixel.

The numerical analysis of the statistical retrieval showed a RMSE between retrieved and true r_{eff} of around $1\,\mu m$ to $1.5\,\mu m$. For the airborne measurement perspective aimed for (see part 2 of this work), the statistical retrieval reliably detects the present effective radius profile, while sanity checks showed no prior bias of the retrieval towards specific cloud droplet size profiles. This is an essential prerequisite for all consecutive interpretation of the retrieval results. Furthermore, the retrieval performance

5   remained the same when faced with unknown cloud side scenes not included in the ensemble used for the retrieval. It can therefore be concluded that the retrieval is not over-fitted and that it represents the statistical relationship between reflected radiance and cloud droplet size for this cloud side perspective.

Limited to optically thick water clouds, this work investigated the main reason for reflectance ambiguities from cloud sides. Within the same 3D cloud side scene, viewing perspectives onto cloud surfaces can be steeper or more oblique as the illumi-

10   nation angle. As a consequence, the correlation between reflected solar radiance pairs and droplet sizes becomes ambiguous.

The next important step is the application of the proposed retrieval technique to real measurements. In combination with simultaneous in-situ measurements, airborne cloud side measurements have been acquired with the hyperspectral cloud and sky imager specMACS. In a follow-up paper part 2, the proposed retrieval will be validated with this independent in-situ data.

A further important point is the development of a distance mapping for the retrieval. The height and location assignment of

15   retrieval results is not just of uttermost importance for the comparison with in situ measurements and models, but also essential to estimate the cloud distance for a potential aerosol correction. Here, first promising results could be achieved by exploiting the oxygen A-band absorption at $\lambda = 762\,nm$ presented in Zinner et al. (2018). In conclusion, the present work developed a working effective radius retrieval to measurements of clouds sides applicable to real measurements and thus paved the way for further research on this topic.

Atmospheric
Measurement
Techniques
Discussions

References

Anderson, G., Clough, S., Kneizys, F., Chetwynd, J., and Shettle, E.: AFGL Atmospheric Constituent Profiles (0-120 km), Tech. Rep. AFGL-TR-86-0110, 1986.

Arabas, S., Pawlowska, H., and Grabowski, W. W.: Effective radius and droplet spectral width from in-situ aircraft observations in trade-wind
5   cumuli during RICO, Geophys. Res. Lett., 36, L11 803, https://doi.org/10.1029/2009GL038257, 2009.

Arking, A. and Childs, J.: Retrieval of cloud cover parameters from multispectral satellite images., Journal of Applied Meteorology, 24, 322–334, 1985.

Bugliaro, L., Zinner, T., Keil, C., Mayer, B., Hollmann, R., Reuter, M., and Thomas, W.: Validation of cloud property retrievals with simulated satellite radiances: a case study for SEVIRI, Atmos. Chem. Phys., 11, 5603–5624, https://doi.org/10.5194/acp-11-5603-2011, http://www.
10   atmos-chem-phys.net/11/5603/2011/, 2011.

Buras, R. and Mayer, B.: Efficient unbiased variance reduction techniques for Monte Carlo simulations of radiative transfer in cloudy atmospheres: the solution, J. Quant. Spectrosc. Radiat. Transfer, 112, 434–447, 2011.

Cahalan, R. F., Ridgway, W., Wiscombe, W., and Bell, T.: The albedo of fractal stratocumulus clouds, Journal of the Atmospheric Sciences, 51, 2434–2455, 1994.

15   Dubovik, O., Herman, M., Holdak, A., Lapyonok, T., Tanré, D., Deuzé, J. L., Ducos, F., Sinyuk, A., and Lopatin, A.: Statistically optimized inversion algorithm for enhanced retrieval of aerosol properties from spectral multi-angle polarimetric satellite observations, Atmos. Meas. Tech., 4, 975–1018, https://doi.org/10.5194/amt-4-975-2011, http://www.atmos-meas-tech.net/4/975/2011/, 2011.

Ehrlich, A., Bierwirth, E., Wendisch, M., Gayet, J.-F., Mioche, G., Lampert, A., and Heintzenberg, J.: Cloud phase identification of Arctic boundary-layer clouds from airborne spectral reflection measurements: test of three approaches, Atmos. Chem. Phys., 8, 7493–7505,
20   https://doi.org/10.5194/acp-8-7493-2008, http://www.atmos-chem-phys.net/8/7493/2008/, 2008.

Eichler, H., Ehrlich, A., Wendisch, M., Mioche, G., Gayet, J.-F., Wirth, M., Emde, C., and Minikin, A.: Influence of ice crystal shape on retrieval of cirrus optical thickness and effective radius: A case study, Journal of Geophysical Research: Atmospheres, 114, D19 203, https://doi.org/10.1029/2009JD012215, http://onlinelibrary.wiley.com/doi/10.1029/2009JD012215/abstract, 2009.

Emde, C., Buras-Schnell, R., Kylling, A., Mayer, B., Gasteiger, J., Hamann, U., Kylling, J., Richter, B., Pause, C., Dowling, T., and
25   Bugliaro, L.: The libRadtran software package for radiative transfer calculations (version 2.0.1), Geosci. Model Dev., 9, 1647–1672, https://doi.org/10.5194/gmd-9-1647-2016, https://www.geosci-model-dev.net/9/1647/2016/, 2016.

Ewald, F.: Implications of cloud geometry for the remote sensing of particle size profiles, Master's thesis, Ludwig–Maximilians–University, 2012.

Ewald, F., Zinner, T., and Mayer, B.: Remote sensing of particle size profiles from cloud sides: Observables and retrievals in a 3D environ-
30   ment, in: AIP Conference Proceedings, vol. 1531, pp. 83–86, AIP Publishing, https://doi.org/10.1063/1.4804713, http://scitation.aip.org/content/aip/proceeding/aipcp/10.1063/1.4804713, 2013.

Ewald, F. and Kölling, T. and Baumgartner, A. and Zinner, T. and Mayer, B.: Design and characterization of specMACS, a multipurpose hyperspectral cloud and sky imager, Atmos. Meas. Tech., 9, 2015–2042, https://doi.org/0.5194/amt-9-2015-2016, 2016.

Feingold, G., Kreidenweis, S. M., Stevens, B., and Cotton, W. R.: Numerical simulations of stratocumulus processing of
35   cloud condensation nuclei through collision-coalescence, Journal of Geophysical Research: Atmospheres, 101, 21 391–21 402, https://doi.org/10.1029/96JD01552, http://onlinelibrary.wiley.com/doi/10.1029/96JD01552/abstract, 1996.

Fischer, J. and Grassl, H.: Detection of Cloud-Top Height from Backscattered Radiances within the Oxygen A Band. Part 1: Theoretical Study, Journal of Applied Meteorology, 30, 1245–1259, https://doi.org/10.1175/1520-0450(1991)030<1245:DOCTHF>2.0.CO;2, http://journals.ametsoc.org/doi/abs/10.1175/1520-0450(1991)030%3C1245:DOCTHF%3E2.0.CO%3B2, 1991.

Gasteiger, J., Emde, C., Mayer, B., Buras, R., Buehler, S. A., and Lemke, O.: Representative wavelengths absorption parameterization applied to satellite channels and spectral bands, Journal of Quantitative Spectroscopy and Radiative Transfer, 148, 99–115, https://doi.org/10.1016/j.jqsrt.2014.06.024, http://www.sciencedirect.com/science/article/pii/S0022407314002842, 2014.

Han, Q., Rossow, W., and Lacis, A.: Near-global survey of effective droplet radii in liquid water clouds using ISCCP data, Journal of Climate, 7, 465–497, 1994.

Hansen, J. and Pollack, J.: Near-infrared light scattering by terrestrial clouds, Journal of the Atmospheric Sciences, 27, 265–281, 1970.

Hess, M., Koepke, P., and Schult, I.: Optical Properties of Aerosols and Clouds: The Software Package OPAC, Bulletin of the American Meteorological Society, 79, 831–844, https://doi.org/10.1175/1520-0477(1998)079<0831:OPOAAC>2.0.CO;2, http://journals.ametsoc.org/doi/abs/10.1175/1520-0477%281998%29079%3C0831%3AOPOAAC%3E2.0.CO%3B2, 1998.

Holben, B., Eck, T., Slutsker, I., Tanre, D., Buis, J., Setzer, A., Vermote, E., Reagan, J., Kaufman, Y., Nakajima, T. Y., Lavenu, F., Jankowiak, I., and Smirnov, A.: AERONET - a federated instrument network and data archive for aerosol characterization, Remote Sens. Environ., 66, 1–16, 1998.

Jäkel, E., Walter, J., and Wendisch, M.: Thermodynamic phase retrieval of convective clouds: impact of sensor viewing geometry and vertical distribution of cloud properties, Atmos. Meas. Tech., 6, 539–547, https://doi.org/10.5194/amt-6-539-2013, http://www.atmos-meas-tech.net/6/539/2013/, 2013.

Jiang, G. M. and Li, Z. L.: Cross-calibration of MSG1-SEVIRI infrared channels with Terra-MODIS channels, Int. J. Remote Sensing, 30, 753–769, https://doi.org/http://dx.doi.org/10.1080/01431160802392638, 2009.

Jiang, H., Feingold, G., Jonsson, H. H., Lu, M.-L., Chuang, P. Y., Flagan, R. C., and Seinfeld, J. H.: Statistical comparison of properties of simulated and observed cumulus clouds in the vicinity of Houston during the Gulf of Mexico Atmospheric Composition and Climate Study (GoMACCS), Journal of Geophysical Research: Atmospheres, 113, D13 205, https://doi.org/10.1029/2007JD009304, http://onlinelibrary.wiley.com/doi/10.1029/2007JD009304/abstract, 2008.

King, M.: A method for determining the single scattering albedo of clouds through observation of the internal scattered radiation field, Journal of the Atmospheric Sciences, 38, 2031–2044, 1981.

King, M.: Determination of the scaled optical thickness of clouds from reflected solar radiation measurements, Journal of the Atmospheric Sciences, 44, 1734–1751, 1987.

King, M., Radke, L., and Hobbs, P.: Determination of the spectral absorption of solar radiation by marine stratocumulus clouds from airborne measurements within clouds, Journal of the Atmospheric Sciences, 47, 894–907, 1990.

King, M., Platnick, S., Yang, P., Arnold, G., Gray, M., Riedi, J., Ackermann, A., and Liou, K.: Remote sensing of liquid water and ice cloud optical thickness and effective radius in the Arctic: Application of airborne multispectral MAS data, Journal of Atmospheric and Oceanic Technology, 21, 857–875, 2004.

Kurucz, R. L.: Synthetic Infrared Spectra, in: Infrared Solar Physics, edited by D. M. Rabin, J. T. Jefferies, & C. Lindsey, vol. 154 of *IAU Symposium*, p. 523, 1994.

Langmore, I., Davis, A., and Bal, G.: Multipixel Retrieval of Structural and Optical Parameters in a 2-D Scene With a Path-Recycling Monte Carlo Forward Model and a New Bayesian Inference Engine, IEEE Transactions on Geoscience and Remote Sensing, 51, 2903–2919, https://doi.org/10.1109/TGRS.2012.2217380, 2013.

Marshak, A., Martins, J. V., Zubko, V., and Kaufman, Y.: What does reflection from cloud sides tell us about vertical distribution of cloud droplet sizes?, Atmospheric Chemistry & Physics, 6, 7207–7233, 2006a.

Marshak, A., Platnick, S., Varnai, T., Wen, G., and Cahalan, R. F.: Impact of three-dimensional radiative effects on satellite retrievals of cloud droplet sizes, Journal of Geophysical Research, 111, D09 207, https://doi.org/10.1029/2005JD006686, 2006b.

5 Martin, G. M., Johnson, D. W., and Spice, A.: The Measurement and Parameterization of Effective Radius of Droplets in Warm Stratocumulus Clouds, Journal of the Atmospheric Sciences, 51, 1823–1842, https://doi.org/10.1175/1520-0469(1994)051<1823:TMAPOE>2.0.CO;2, http://journals.ametsoc.org/doi/abs/10.1175/1520-0469(1994)051%3C1823:TMAPOE%3E2.0.CO;2, 1994.

Martin, W., Cairns, B., and Bal, G.: Adjoint methods for adjusting three-dimensional atmosphere and surface properties to fit multi-angle/multi-pixel polarimetric measurements, Journal of Quantitative Spectroscopy and Radiative Transfer, 144, 68–85,
10 https://doi.org/10.1016/j.jqsrt.2014.03.030, http://www.sciencedirect.com/science/article/pii/S002240731400154X, 2014.

Martins, J., Marshak, A., Remer, L., Rosenfeld, D., Kaufman, Y., Fernandez-Borda, R., Koren, I., Correia, A., Zubko, V., and Artaxo, P.: Remote sensing the vertical profile of cloud droplet effective radius, thermodynamic phase, and temperature, Atmos. Chem. Phys, 11, 9485–9501, 2011.

Mayer, B. and Kylling, A.: Technical note: The libRadtran software package for radiative transfer calculations - description and examples of
15 use, 5, 1855–1877, 2005.

Mayer, B.: MYSTIC, Monte Carlo code for the physically correct tracing of photons in cloudy atmospheres, 1998.

Mayer, B.: Radiative transfer in the cloudy atmosphere, European Physical Journal Conferences, 1, 75–99, 2009.

McBride, P. J., Schmidt, K. S., Pilewskie, P., Kittelman, A. S., and Wolfe, D. E.: A spectral method for retrieving cloud optical thickness and effective radius from surface-based transmittance measurements, Atmos. Chem. Phys., 11, 7235–7252, https://doi.org/10.5194/acp-
20 11-7235-2011, http://www.atmos-chem-phys.net/11/7235/2011/, 2011.

McFarlane, S., Evans, K., and Ackerman, A.: A Bayesian algorithm for the retrieval of liquid water cloud properties from microwave radiometer and millimeter radar data, J. Geophys. Res, 107, 10.1029, 2002.

Mosegaard, K. and Tarantola, A.: Monte Carlo sampling of solutions to inverse problems, Journal of Geophysical Research: Solid Earth, 100, 12 431–12 447, https://doi.org/10.1029/94JB03097, http://onlinelibrary.wiley.com/doi/10.1029/94JB03097/abstract, 1995.

25 Nakajima, T. Y. and King, M. D.: Determination of the optical thickness and effective particle radius of clouds from reflected solar radiation measurements. Part I: Theory, J. Atmos. Sci, 47, 1878–1893, 1990.

POkamura, R. and Iwabuchi, H. and Schmidt, K. S.: Feasibility study of multi-pixel retrieval of optical thickness and droplet effective radius of inhomogeneous clouds using deep learning, Atmos. Meas. Tech., 10, https://doi.org/10.5194/amt-10-4747-2017, 4747–4759, 2017.

Pilewskie, P., Pommier, J., Bergstrom, R., Gore, W., Rabbette, M., Schmid, B., Hobbs, P. V., and Tsay, S. C.: Solar spectral radiative forcing
30 during the Southern African regional science initiative, J. Geophys. Res., 108, doi:10.1029/2002JD002 411, 2003.

Plass, G. N. and Kattawar, G. W.: Influence of Single Scattering Albedo on Reflected and Transmitted Light from Clouds, Applied Optics, 7, 361–367, https://doi.org/10.1364/AO.7.000361, http://ao.osa.org/abstract.cfm?URI=ao-7-2-361, 1968.

Platnick, S.: Vertical photon transport in cloud remote sensing problems, Journal of Geophysical Research, 105, 22 919–22 935, 2000.

Platnick, S., Li, J., King, M. D., Gerber, H., and Hobbs, P.: A solar reflectance method for retrieving the optical thickness and droplet size of
35 liquid water clouds over snow and ice surfaces, Journal of Geophysical Research, 106, 15, 2001.

Rauber, R. M., Ochs, H. T., Di Girolamo, L., Göke, S., Snodgrass, E., Stevens, B., Knight, C., Jensen, J. B., Lenschow, D. H., Rilling, R. A., Rogers, D. C., Stith, J. L., Albrecht, B. A., Zuidema, P., Blyth, A. M., Fairall, C. W., Brewer, W. A., Tucker, S., Lasher-Trapp, S. G., Mayol-Bracero, O. L., Vali, G., Geerts, B., Anderson, J. R., Baker, B. A., Lawson, R. P., Bandy, A. R., Thornton, D. C., Burnet, E.,

Brenguier, J.-L., Gomes, L., Brown, P. R. A., Chuang, P., Cotton, W. R., Gerber, H., Heikes, B. G., Hudson, J. G., Kollias, P., Krueger, S. K., Nuijens, L., O'Sullivan, D. W., Siebesma, A. P., and Twohy, C. H.: Rain in Shallow Cumulus Over the Ocean: The RICO Campaign, Bulletin of the American Meteorological Society, 88, 1912–1928, https://doi.org/10.1175/BAMS-88-12-1912, http://journals.ametsoc.org/doi/abs/10.1175/BAMS-88-12-1912, 2007.

5 Roebeling, R. A., Feijt, A. J., and Stammes, P.: Cloud property retrievals for climate monitoring: Implications of differences between Spinning Enhanced Visible and Infrared Imager (SEVIRI) on METEOSAT-8 and Advanced Very High Resolution Radiometer (AVHRR) on NOAA-17, Journal of Geophysical Research, 111, D20 210, https://doi.org/10.1029/2005JD006990, 2006.

Rosenfeld, D., Williams, E., Andreae, M. O., Freud, E., Pöschl, U., and Rennó, N. O.: The scientific basis for a satellite mission to retrieve CCN concentrations and their impacts on convective clouds, Atmos. Meas. Tech., 5, 2039–2055, https://doi.org/10.5194/amt-5-2039-2012,
10   http://www.atmos-meas-tech.net/5/2039/2012/, 2012.

Rothman, L. S., Jacquemart, D., Barbe, A., Benner, D. C., Birk, M., Brown, L. R., Carleer, M. R., Chackerian Jr., C., Chance, K., Coudert, L. H., Dana, V., Devi, V. M., Flaud, J. ., Gamache, R. R., Goldman, A., Hartmann, J. ., Jucks, K. W., Maki, A. G., Mandin, J. ., Massie, S. T., Orphal, J., Perrin, A., Rinsland, C. P., Smith, M. A. H., Tennyson, J., Tolchenov, R. N., Toth, R. A., Vander Auwera, J., Varanasi, P., and Wagner, G.: The HITRAN 2004 molecular spectroscopic database, Journal of Quantitative Spectroscopy and Radiative Transfer, 96,
15   139–204, 2005.

Rozanov, V., Kokhanovsky, A., and Burrows, J.: The determination of cloud altitudes using GOME reflectance spectra: multilayered cloud systems, IEEE Transcations on Geoscience and Remote Sensing, 42, 1009–1017, 2004.

Schmidt, K., Pilewskie, P., Platnick, S., Wind, G., Yang, P., and Wendisch, M.: Comparing irradiance fields derived from Moderate Resolution Imaging Spectroradiometer airborne simulator cirrus cloud retrievals with solar spectral flux radiometer measurements, J. Geophys. Res,
20   112, D24 206, 2007.

Scott, D. W., Tapia, R. A., and Thompson, J. R.: Kernel density estimation revisited, Nonlinear Analysis: Theory, Methods & Applications, 1, 339–372, https://doi.org/10.1016/S0362-546X(97)90003-1, http://www.sciencedirect.com/science/article/pii/S0362546X97900031, 1977.

Stamnes, K., Tsay, S.-C., Wiscombe, W., and Jayaweera, K.: A numerically stable algorithm for discrete-ordinate-method radiative transfer
25   in multiple scattering and emitting layered media, Applied Optics, 27, 2502–2509, 1988.

Twomey, S. and Cocks, T.: Remote sensing of cloud parameters from spectral reflectance in the near-infrared, Beiträge zur Physik der Atmosphäre, 62, 172–179, 1989.

Tzivion, S., Feingold, G., and Levin, Z.: An Efficient Numerical Solution to the Stochastic Collection Equation, Journal of the Atmospheric Sciences, 44, 3139–3149, https://doi.org/10.1175/1520-0469(1987)044<3139:AENSTT>2.0.CO;2, http://journals.ametsoc.org/
30   doi/abs/10.1175/1520-0469(1987)044%3C3139%3AAENSTT%3E2.0.CO%3B2, 1987.

Tzivion, S., Feingold, G., and Levin, Z.: The Evolution of Raindrop Spectra. Part II: Collisional Collection/Breakup and Evaporation in a Rainshaft, 46, 3312–3328, https://doi.org/10.1175/1520-0469(1989)046<3312:TEORSP>2.0.CO;2, 1989.

van Diedenhoven, B., Hasekamp, O. P., and Landgraf, J.: Retrieval of cloud parameters from satellite-based reflectance measurements in the ultraviolet and the oxygen A-band, Journal of Geophysical Research: Atmospheres, 112, D15 208, https://doi.org/10.1029/2006JD008155,
35   http://onlinelibrary.wiley.com/doi/10.1029/2006JD008155/abstract, 2007.

Vant-Hull, B., Marshak, A., Remer, L., and Li, Z.: The effects of scattering angle and cumulus cloud geometry on satellite retrievals of cloud droplet effective radius, Geoscience and Remote Sensing, IEEE Transactions on, 45, 1039–1045, 2007.

Atmospheric
Measurement
Techniques
Discussions

Varnai, T. and Marshak, A.: Observations of the three-dimensional radiative effects that influence MODIS cloud optical thickness retrievals, Journal of the Atmospheric Sciences, 59, 1607–1618, 2002.

Varnai, T. and Marshak, A.: A method for analyzing how various parts of clouds influence each other's brightness, Journal of Geophysical Research, 108, 4706, https://doi.org/10.1029/2003JD003561, 2003.

5   Varnai, T. and Marshak, A.: View angle dependence of cloud optical thicknesses retrieved by Moderate Resolution Imaging Spectroradiometer (MODIS), Journal of Geophysical Research, 112, D06 203, https://doi.org/10.1029/2005JD006912, 2007.

Varnai, T. and Marshak, A.: MODIS observations of enhanced clear sky reflectance near clouds, Geophys. Res. Lett., 36, L06 807, https://doi.org/10.1029/2008GL037089, 2009.

Warner, J.: The Water Content of Cumuliform Cloud, Tellus, 7, 449–457, https://doi.org/10.1111/j.2153-3490.1955.tb01183.x, http://
10   onlinelibrary.wiley.com/doi/10.1111/j.2153-3490.1955.tb01183.x/abstract, 1955.

Wen, G., Marshak, A., Cahalan, R. F., Remer, L. A., and Kleidman, R. G.: 3-D aerosol-cloud radiative interaction observed in collocated MODIS and ASTER images of cumulus cloud fields, Journal of Geophysical Research, 112, D13 204, https://doi.org/10.1029/2006JD008267, 2007.

Wendisch, M., Müller, D., Schell, D., and Heintzenberg, J.: An airborne spectral albedometer with active horizontal stabilization, Journal of
15   Atmospheric and Oceanic Technology, 18, 1856–1866, 2001.

Wendisch, M. and Mayer, B.: Vertical distribution of spectral solar irradiance in the cloudless sky - A case study, Geophys. Res. Lett., 30, doi:10.1029/2002GL016 529, 2003.

Wendisch, Manfred and Pöschl, Ulrich and Andreae, Meinrat O. and Machado, Luiz A. T. and Albrecht, Rachel and Schlager, Hans and Rosenfeld, Daniel and Martin, Scot T. and Abdelmonem, Ahmed and Afchine, Armin and Araùjo, Alessandro C. and Artaxo, Paulo and
20   Aufmhoff, Heinfried and Barbosa, Henrique M. J. and Borrmann, Stephan and Braga, Ramon and Buchholz, Bernhard and Cecchini, Micael Amore and Costa, Anja and Curtius, Joachim and Dollner, Maximilian and Dorf, Marcel and Dreiling, Volker and Ebert, Volker and Ehrlich, André and Ewald, Florian and Fisch, Gilberto and Fix, Andreas and Frank, Fabian and Fütterer, Daniel and Heckl, Christopher and Heidelberg, Fabian and Hüneke, Tilman and Jäkel, Evelyn and Järvinen, Emma and Jurkat, Tina and Kanter, Sandra and Kästner, Udo and Kenntner, Mareike and Kesselmeier, Jürgen and Klimach, Thomas and Knecht, Matthias and Kohl, Rebecca and Kölling, Tobias
25   and Krämer, Martina and Krüger, Mira and Krisna, Trismono Candra and Lavric, Jost V. and Longo, Karla and Mahnke, Christoph and Manzi, Antonio O. and Mayer, Bernhard and Mertes, Stephan and Minikin, Andreas and Molleker, Sergej and Münch, Steffen and Nillius, Björn and Pfeilsticker, Klaus and Pöhlker, Christopher and Roiger, Anke and Rose, Diana and Rosenow, Dagmar and Sauer, Daniel and Schnaiter, Martin and Schneider, Johannes and Schulz, Christiane and de Souza, Rodrigo A. F. and Spanu, Antonio and Stock, Paul and Vila, Daniel and Voigt, Christiane and Walser, Adrian and Walter, David and Weigel, Ralf and Weinzierl, Bernadett and Werner, Frank
30   and Yamasoe, Marcia A. and Ziereis, Helmut and Zinner, Tobias and Zöger, Martin: ACRIDICON–CHUVA Campaign: Studying Tropical Deep Convective Clouds and Precipitation over Amazonia Using the New German Research Aircraft HALO, Bulletin of the American Meteorological Society, 18, 1885–1908, https://doi.org/10.1175/BAMS-D-14-00255.1, 2016.

Wiscombe, W. and Warren, S.: A Model for the Spectral Albedo of Snow. I: Pure Snow, Journal of the Atmospheric Sciences, 37, 2712–2733, 1980.

35   Yang, P., Wei, H., Baum, B., Huang, H., Heymsfield, A., Hu, Y., Gao, B., and Turner, D.: The spectral signature of mixed-phase clouds composed of non-spherical ice crystals and spherical liquid droplets in the terrestrial window region, Journal of Quantitative Spectroscopy and Radiative Transfer, 79, 1171–1188, 2003.

Yuter, S. E. and Houze, R. A.: Three-Dimensional Kinematic and Microphysical Evolution of Florida Cumulonimbus. Part II: Frequency Distributions of Vertical Velocity, Reflectivity, and Differential Reflectivity, Monthly Weather Review, 123, 1941–1963, https://doi.org/10.1175/1520-0493(1995)123<1941:TDKAME>2.0.CO;2, http://journals.ametsoc.org/doi/abs/10.1175/1520-0493(1995) 123%3C1941%3ATDKAME%3E2.0.CO%3B2, 1995.

5 Zinner, T. and Mayer, B.: Remote sensing of stratocumulus clouds: Uncertainties and biases due to inhomogeneity, Journal of Geophysical Research, 111, D14 209, https://doi.org/10.1029/2005JD006955, 2006.

Zinner, T., Marshak, A., Lang, S., Martins, J. V., and Mayer, B.: Remote sensing of cloud sides of deep convection: towards a three-dimensional retrieval of cloud particle size profiles, Atmos. Chem. Phys., 8, 4741–4757, 2008.

Zinner, T., Schwarz, U., Kölling, T., Ewald, F., Jäkel, E., Mayer, B., and Wendisch, M.: Cloud geometry from oxygen-A band observations

10 through an aircraft side window, Atmos. Meas. Tech. Diss., submitted, 2018.